The Influence of Lateral and Top Boundary Conditions on Regional Air Quality Prediction: a Multi-Scale Study Coupling Regional and Global Chemical Transport Models

Youhua Tang[1] (ytang@cgrer.uiowa.edu), Gregory R. Carmichael[1] (gcarmich@engineering.uiowa.edu), Narisara Thongboonchoo[1] (nthongbo@cgrer.uiowa.edu), Tianfeng Chai[1] (tchai@cgrer.uiowa.edu), Larry W. Horowitz[2] (larry.horowitz@noaa.gov), Robert B. Pierce[3] (r.b.pierce@larc.nasa.gov), Jassim A. Al-Saadi[3] (j.a.al-saadi@nasa.gov), Gabriele Pfister[4] (pfister@ucar.edu), Jeffrey M. Vukovich[5] (jeff_vukovich@unc.edu), Melody A. Avery[3] (m.a.avery@larc.nasa.gov), Glen W. Sachse[3] (g.w.sachse@larc.nasa.gov), Thomas B. Ryerson[6] (thomas.b.ryerson@noaa.gov), John S. Holloway[6] (John.S.Holloway@noaa.gov), Elliot L. Atlas[7] (eatlas@rsmas.miami.edu), Frank M. Flocke[4] (ffl@ucar.edu), Rodney J. Weber[8] (rweber@eas.gatech.edu), L. Gregory Huey[8] (greg.huey@eas.gatech.edu), Jack E. Dibb[9] (jack.dibb@unh.edu), David G. Streets[10] (dstreets@anl.gov), and William H. Brune[11] (brune@ems.psu.edu)

1. Center for Global and Regional Environmental Research, University of Iowa, Iowa City, Iowa, USA
2. NOAA GFDL Laboratory, Princeton, New Jersey, USA
3. NASA Langley Research Center, Virginia, USA
4. National Center for Atmospheric Research, Boulder, Colorado, USA
5. Carolina Environmental Program (CEP), University of North Carolina at Chapel Hill
6. NOAA Aeronomy Laboratory, Boulder, Colorado, USA
7. University of Miami, Miami, Florida, USA
8. Georgia Institute of Technology, Atlanta, Georgia, USA
9. University of New Hampshire, Durham, NH, USA
10. Argonne National Laboratory, Argonne, Illinois, USA
11. Pennsylvania State University, University Park, PA, USA

Abstract:

We studied the sensitivity of regional air quality model to various lateral and top boundary conditions in 2 scales: 60km domain covering the whole USA and the 12km domain over Northeastern USA. Three global models (MOZART-NCAR, MOZART-GFDL and RAQMS) were used to drive the STEM-2K3 regional model with time-varied lateral and top boundary conditions (BCs). The regional simulations with different global BCs were examined using ICARTT aircraft measurements performed in the summer of 2004, and the simulations were shown to be sensitive to the boundary conditions from the global models, especially for relatively long-lived species, like CO and O_3. For example,

differences in the mean CO concentrations from 3 different global-model boundary conditions were as large as 50 ppbv. Over certain model grids, the model's sensitivity to BCs is found to depend not only on the distance from the domain's top and lateral boundaries, downwind/upwind situation, but also on regional emissions and species properties. The near-surface prediction over polluted area is usually not as sensitive to the variation of BCs, but to the magnitude of their background concentrations. We also tested the sensitivity of model to temporal and spatial variations of the BCs by comparing the simulations with time-varied BCs to the corresponding simulations with time-mean and profile BCs. The time-varied BCs provided by the external models usually yielded better results compared to observation. The effect of model resolution on the BC sensitivity was also studied. For most species, the model's sensitivity to BCs also showed strong altitude dependence.

1. Introduction

Regional models require appropriate lateral and top boundary conditions (BCs) to achieve reasonable predictions. Mesoscale meteorological models, like MM5, RAMS and WRF, usually use global meteorological model as their lateral boundary conditions. In principle, regional chemical transport/air quality model should also import boundary conditions from corresponding global models to consider the external forcing. However, additional uncertainties are introduced in this importing process due to the uncertainties in the global models and differences in resolution et al. In the past, most regional chemical transport models use fixed concentration profiles as their boundary conditions. These concentration profiles should represent the mean concentrations during the period of interest. Some profiles are based on historical measurements (Winner et al., 1995), and some profiles are set to typical clean concentrations (Chen et al., 2003). It should be noted that most profiles boundary conditions lack temporal and spatial variations, and thus the corresponding simulation mainly reflects the contribution of pollutant emissions within the model domain.

The ICARTT (International Consortium for Atmospheric Research on Transport and Transformation) field experiment was performed in summer, 2004 (http://www.al.noaa.gov/ICARTT/), including NASA INTEX-A (Intercontinental Chemical Transport Experiment -A), NOAA NEAQS/ITCT-2k4 (New England Air Quality Study - Intercontinental Transport and Chemical Transformation, 2004) and other coordinated studies. During the ICARTT period, NASA DC-8 aircraft performed 18 research flights covering the continental USA, and NOAA WP-3 aircraft also had 18 research flights mainly over northeastern USA. Some of these flights encountered remote signatures, such as Asian air masses, long-range transported biomass burning plume, and stratospheric airmass intrusion. Normal tropospheric regional chemical transport model can not predict these phenomena without appropriate lateral and top boundary conditions. The ICARTT airborne measurements provide us an opportunity to examine the performance of regional model driven by different boundary conditions from different global models. We can also test the dependence of regional model on BCs under different scales.

In this study, we evaluate the sensitivity and performance of rregional model predictions to various BC treatments. we specifically employed regional chemical transport model STEM-2K3 (Tang et al., 2004) with lateral and top boundary conditions from three global models: MOZART-NCAR, MOZART-GFDL and RAQMS. Figure 1 shows the framework of this study. The detail of these models will be described later. The STEM model provides predictions in two horizontal resolutions: 60km and 12km. We will study sensitivity of model to simulating scale with these model results.

2. Methodology Description

In this study, we employed STEM-2K3 (Tang et al., 2004) regional chemical transport model. The STEM-2K3 model is a flexible regional-scale chemical transport model using SAPRC99 chemical mechanism (Cater, 2000) with on-line photolysis solver (Tang et al, 2003a). Its aerosol solver is SCAPE II. In this study, MM5 driven by NCEP FNL (Final Global Data Assimilation System) 1°×1° analyzed data provides meteorological field.

The MM5 simulation was performed in a 60km domain covering North American, and a one-way nested 12km domain that covered Northeastern USA (Figure 2), with sigma layers extending from surface to 100hPa: 0.999, 0.9965, 0.9925, 0.985, 0.97, 0.945, 0.91, 0.87, 0.825, 0.77, 0.71, 0.65, 0.59, 0.53, 0.47, 0.41, 0.35, 0.285, 0.21, 0.125, and 0.04. The FNL data (1°×1° every 6 hours) was used to drive MM5 simulations. Grid nudging was performed every 6 hours, and re-initialization with FNL data took place every 72 hours. The cloud scheme of Grell et al. (1994) was chosen for the physical parameterization, and MRF scheme (Hong and Pan, 1996) was employed for PBL parameterization.

2.1 Emissions

During the ICARTT field experiment the U.S. EPA National Emission Inventory (NEI) with base year 1999 was used for forecasting. In this study, the NEI-2001 emission is employed. It should be noted that NEI-2001 and NEI-1999 emissions differ significantly in CO, NO_x and SO_2, and the difference between the forecast and post simulation are mainly due to the emission differences. However, even the NEI-2001 emission does not accurately represent the field data in ICARTT experiment in 2004. For examples, the NEI-2001 inventory tends to systematically underestimate lighter alkanes but overpredict aromatics. In this study, we adjusted VOC emission ratios based on NEI-2001 inventory.

Lightning NOx emission is explicitly treated in this study using data from National Lightning Detection Network (NLDN). NLDN data includes hourly lightning location, signal strength and multiplicity in strokes/flash. We use the method of Price et al. (1997) to derive the lightning NOx emission. Here we use MM5's meteorological information (cloud water content and temperature) to identify the existence of cloud, cloud top and cloud freezing level (Pickering et al., 1998). The cloud-to-ground (CG) flash is the major source of lightning NO_x here, but intra-cloud (IC) also contributes to NO_x source. The IC/CG ratio is an important factor. Here we adopted the method of Pickering et al. (1998) and Price et al. (1997) and the CG fraction in total flashes becomes:

$$P = 1/(z+1)$$
$$z = 0.021(\Delta H)^4 - 0.648(\Delta H)^3 + 7.493(\Delta H)^2 - 36.54(\Delta H) + 63.09$$

where ΔH is thickness in unit km from cloud freezing level to cloud top, which are derives from MM5's meteorological field. This equation can be applied to cold cloud whose ΔH is higher than 5.5km, but less than 14km (Price et al., 1997). In the vertical direction, CG lightning NO_x is uniformly distributed from cloud top to ground. The breakthrough potential of the intra-cloud lightning is 1/10 of CG lightning (Price et al., 1997). We set the negative CG lightning NO_x producing rate to 1×10^{17} molecules/J and Positive CG lightning can generate 1.6 times NO_x as negative CG lightning (Price et al., 1997).

Biogenic emission inventory system 2 (BEIS 2) (Geron, et al., 1994) is used to generate time-varied isoprene and monoterpene emissions driven by MM5's meteorological field. During the ICARTT period, forest fires occurred in Alaska and Northwestern Canada, which is out of our model domain. However, the lateral boundary conditions from global models provide time-varied biomass burning (BB) CO and other species.

Sea salt emissions were estimated using the Gong et al (2003) method driven by MM5's 10m wind speed. In this study, size-resolved sea salt emissions enter 4 aerosol size bins (in diameter): 0.1μm-0.3μm, 0.3μm-1.0μm, 1.0μm-2.5μm, and 2.5μm-10μm (Tang et al., 2004).

2.2 Top and Lateral Boundary Conditions

We have three global model products: MOZART-NCAR (National Center for Atmospheric Research), MOZART-GFDL (NOAA GFDL laboratory) and RAQMS (NASA Langley Research Center). MOZART (Model for OZone And Related chemical Tracers) is a global chemical transport model (Horowitz et al., 2003). Here we implement two MOZART simulations, by NCAR and NOAA/GFDL, respectively. These two MOZART simulations use different configurations: MOZART-NCAR was run by

Gabriele Pfister with 2.8 degree horizontal resolution and MOPITT satellite derived forest fire emissions (Pfister et al, 2005); MOZART-GFDL was run by Larry Horowitz with 1.89 degree horizontal resolution, NCEP reanalysis meteorology, stratospheric O_3 relaxed to climatology, EDGAR Version 2 (1990) (Olivier and Berdowski, 2001) fossil fuel emissions and forest fire emission estimated by Harvard University (Turquety et al., 2005). RAQMS (Regional Air Quality Modeling System) is multi-scale chemical transport model that can run either globally or regionally (Pierce et al., 2003). During the ICARTT period, RAQMS was run globally at 1.4 degree horizontal resolution. The MOZART-NCAR's top boundary differs from the other two simulations. MOZART-NCAR uses a synthetic ozone ("SYNOZ") representation (McLinden et al., 2000) in order to constrain the stratospheric flux of ozone (Emmons et al., in preparation). This causes the reported O_3 species in the model to be underestimated in the upper troposphere. This treatment for O_3 top boundary will result in relatively lower O_3 top boundary conditions compared to the other two models (we will discuss later).

In this study, we imported time-dependent top and lateral boundary conditions for STEM-2k3 from the three global models. Figure 2 shows the mean O_3 top boundary conditions from the three global models used by STEM. STEM's top is the same as the top of MM5: 100 hPa in MM5's reference atmosphere. Figure 2 also shows the STEM primary domain: 97×62 grids in 60km horizontal resolution. As shown in Figure 2, RAQMS provides the highest O_3 top boundary, and MOZART-GFDL ranks the second, which is similar to RAQMS. However, the MOZART-NCAR's top boundary is significantly lower than the other two models by up to 100-200 ppbv, especially north of 40°N.

Figure 3 shows the corresponding CO lateral boundary conditions from the 3 global models. RAQMS tends to yield 20-40 ppbv lower CO concentrations than the two MOZART models in the south and east boundaries of the STEM 60km domain. Among these three lateral boundary conditions, MOZART-GFDL has the highest mean CO concentrations, and especially it has a higher CO west boundary condition, the major inflow boundary, than the other global models. All these models have relatively high CO

concentrations in the north boundary condition, which mainly come from the forest fire emissions in Alaska and Canada. MOZART-GFDL has the highest BB CO concentration among these 3 models, and high CO concentration extend from the surface to about 6km. RAQMS's mean CO concentration in the north boundary is similar to MOZART-GFDL, but has a relatively narrow high-CO plume. MOZART-NCAR shows an isolated CO hot spot at the altitude of 7km.

It should be noted that both Figures 2 and 3 illustrate the period-mean boundary conditions from the three global models. During certain periods, these differences can be much greater. In fact, for other chemical species, these differences can also be higher, too. Since the purpose of this study is not showing the difference among the global models, we will focus on comparing results for the different STEM BCs.

3. Comparison of Different Boundary Conditions

In this study, we perform three STEM regional simulations driven by the three boundary conditions, and compared these simulations with aircraft measurements for the ICARTT period. The three STEM simulations use the same emission and settings except for their top and lateral boundary conditions. At first, we present results for specific ICARTT flights to evaluate the sensitivity of BCs on predictions under specific conditions.

3.1 DC-8 flight on July 15

The 8th DC-8 flight is a transit research flight from St. Louis to New Hampshire. This flight encountered the forest fire plume from Alaska and Northwestern Canada at around 16 UTC. Figure 4 shows the comparison of CO and O_3 between the observation and the simulations with the three boundary conditions. Figure 5A shows the flight path. The STEM simulations with MOZART-GFDL and RAQMS BCs tend to overestimate O_3 concentrations for altitudes > 6km, and the simulation with MOZART-NCAR produced the values closest to the observation. Since all the STEM simulations use the same emission and other settings, this difference come from the differences in the top and

lateral boundary conditions. It should be noted that the O_3 overestimations of MOZART-GFDL and RAQMS in this event are not systemic, and later we will see their performances in other scenarios. Figure 4 shows that the simulated CO with RAQMS BCs is similar to that with MOZART-GFDL BCs, and higher than that with MOZART-NCAR BCs. These differences are consistent with the differences in the corresponding BC concentrations (Figure 2). During the flight segment 15-16UTC, the DC-8 aircraft encountered a forest fire plume emitted from Alaska and Northwestern Canada, and observed CO concentrations increased along with the altitude. Figure 4 shows that none of these simulation completely captured this feature. However, all the CO simulations show slight enhancement around 15:10UTC, implying that they captured part of this feature though the enhancement is not as strong and broad as the measurements due to the coarse resolution of the global models and an underestimation of the forest fire emissions. The CO simulation with RAQMS BCs best matched the observed CO for most flight segments, but it obviously overestimated CO from 16:00UTC to 16:50UTC for this case.

Figure 5 shows the STEM simulated O_3 and CO concentrations in the model's 10km layer with the three global BCs. This DC-8 flight passed through a trough. During the flight segment 13 –19 UTC, the aircraft encountered northwest winds. The simulation with MOZART-NCAR top boundary conditions yielded much lower O_3 concentrations than those with MOZART-GFDL and RAQMS. In the 10km layer, the simulation with MOZART-NCAR BCs does not have O_3 concentrations over 160 ppbv, but the other two simulations yield O_3 concentrations > 200 ppbv. In the northwestern corner, the RAQMS BCs yields O_3 > 250 ppbv. Although these simulations have different O_3 concentrations, their distributions are similar: the high-concentration center is around 85°W, 42°N. Figure 5 D, E, and F shows the corresponding CO concentrations in the three simulations. The simulated CO with MOZART-NCAR BCs is about 20 ppbv lower than the other two simulations in the whole field. RAQMS tends to have lower CO contrast than the two MOZART models in STEM's inflow lateral boundary. In the air stream from the northwest direction (western side of the trough), the simulations with MOZART-NCAR and MOZAR-GFDL BCs have CO enhancements > 20 ppbv compared with their own

backgrounds (Figure 5D, 5E), but the corresponding CO enhancement in the simulation with RAQMS BCs is less than 10 ppbv (Figure 5F).

This comparison shows that the STEM model is very sensitive to external CO and O_3 concentrations in the 10km layer. STEM predicted CO concentrations are determined by the lateral boundary conditions, and its O_3 predictions rely on both top and lateral boundary conditions. Figure 4 show that the three simulations have similar low-altitude O_3 concentrations though their high-altitude concentrations differ significantly. On the other hand, the CO concentration differences keep the nearly same pattern in high and low altitudes. It is imply that high-altitude O_3 prediction could be more sensitive to top boundary conditions due to the stratospheric influence.

3.2 WP-3 flight on July 28

Most NOAA WP-3 flights during the ICARTT period departed from Portsmouth, New Hampshire. In July 28, the WP-3 aircraft performed a south-north flight to eastern Canada and back (Figure 6A). During this flight, the aircraft encountered western and southwestern airflows in the middle altitude. Figure 6 shows the O_3 and CO concentrations in the 5.6km layer by the three simulations driven by the three boundary conditions. The simulation with RAQMS BCs has the highest O_3 among the three simulations in this layer. It should be noted that this difference could not come from surface emission because we applied the same emissions and other settings to these simulations except for the lateral and top boundary conditions. In this event, most of the differences come from the northern lateral boundary. Figure 7 illustrates the simulations compared with the measurement. For the flight segments just after the takeoff and before the landing, there is little difference in the predictions for O_3, CO and NO_y, reflecting the importance of regional and local emissions. The simulations driven by MOZART-GFDL and RAQMS BCs overpredicted the forest fire plume from northwestern Canada (Figure 7), with relative CO enhancement up to 150 ppbv around 16UTC (Figure 7 and Figure 6D). For the same plume, the simulation with MOZART-NCAR BCs show a CO enhancement closer to that observed, but it underestimated the second CO spike around

16:40UTC, while other two models performed better for the second CO enhancement. Both MOZART-GFDL and RAQMS slightly overpredicted the CO background concentration. NO_x tends to be co-emitted with CO from forest fires and is correlated to variety of species comprising NO_y during its transformation (Tang et al, 2003b). Thus NO_y is a relatively long-lived BB tracer. Figure 7 shows that observed NO_y has a similar variation to CO from 15 to 17 UTC, and MOZART-NCAR best captured the NO_y signal of this BB plume. The simulation with RAQMS BCs has the best performance for capturing O_3 inflow event for this period (Figure 6 and Figure 7). Figure 7 shows that two O_3 peaks at around 15:30 UTC and 17:10 UTC were captured by the simulation with RAQMS BCs.

These comparisons along the flight paths show that the regional model's dependence on the top and lateral boundary conditions provided by the three global models. Most differences among these simulations appear in the area near the inflow boundary, such as the north and west borders, or at high altitudes affected by top boundary conditions. In this study, the STEM regional model shows strong dependence on the lateral and top boundary conditions.

4. Influence of Temporal and Spatial Variations of Boundary Conditions

We have discussed the impact of different boundary conditions imported from different global models. However, this impact just reflects the influence due to different coupled models. Some regional air quality models use predefined profiles as boundary conditions, which differ from the case we discussed above. Predefined profile BCs are designed t yield reasonable background concentrations for long-lived species, but lack of temporal and spatial variations. Under some situations for some species, the magnitude of the background concentration is much greater than its spatial and temporal variations, and these variations become less important for certain predictions. This is the reason that

predefined profile BCs are useful in regional air quality prediction. In this study, we employ simulations in two scales: 60km and 12km, to test the impact of fixed BCs.

Figure 1 shows the framework of this study. Here we use the STEM 60km simulation with MOZART-NCAR BCs as the base case. By performing a temporal average of the lateral and top BCs provided by MOZART-NCAR, we get the temporal mean BCs for the 60km domain. Through further horizontal averaging of the time-mean lateral boundary condition along its south, north, east and west boundaries, respectively, we get the profile-equivalent lateral BCs, which is identical to the BCs predefined by 4 profiles for each species. With these three BCs (original time-varying, time-mean, and profile), we have 3 corresponding simulations in the 60km domain. The simulation with profile BCs uses the same top BC as that with time-mean BCs. We also performed 3 simulations with the one-way nested 12km domain covering the Northeastern United States, using original, time-fixed and profile BCs derived from the 60km simulation with the original MOZART-NCAR BCs (Figure 1). Through comparing these simulations, we can test the model's sensitivity to temporal and spatial variation of BCs at different scales. During the ICARTT period, the NASA DC-8 flights covered nearly the whole continental USA in a large scale, and the NOAA WP-3 flights mainly flew over Northeastern USA and surrounding area and captured more of the fine structure of urban plumes. In this section, we compare the 60km simulations to the DC-8 airborne measurements, and the 12km simulations to the WP-3 observations.

4.1 DC-8 and WP-3 flights on July 31

Both the NASA DC-8 and NOAA WP-3 aircrafts had flights on July 31. The DC-8 aircraft headed to the central North Atlantic and flew back to New Hampshire. Figure 8A shows the 60km CO simulations compared to the aircraft measurement for the returning segment after 21.5 UTC, and the corresponding flight path is shown in Figure 8B. Both the simulations with time-mean and profile BCs tend to overpredict CO by 10-20 ppbv, and the simulation with the original MOZART-NCAR BCs has the best result compared to the measurement. The prediction bias in the profile-BCs simulation is higher than that

in time mean BCs. Air masses encountered by this flight mainly come from south and southwest directions (Figure 8). The CO simulation in the 3km layer with original BCs shows that the inflow CO concentration near the southern inflow boundary region affected this flight is around 70-80ppbv. The simulated CO with time-mean BCs is about 5-20 ppbv higher than that with the original BCs near the southern inflow boundary, and the corresponding difference between the original and profile BCs is even higher. In fact, this flight did not encounter the biggest CO difference near northern inflow boundary, which is up to 70 ppbv in the 3km layer. All the biggest differences were brought by the strong inflow from the lateral boundaries.

On the same day, the NOAA WP-3 aircraft performed a nighttime flight over New England area and sampled the Boston plume. Figure 9 shows the 12km simulated CO and O_3 concentrations compared to aircraft observation for the segment 23-25 UTC. This flight segment is shown in Figure 10, which also shows the nested 12km domain. During this flight, the aircraft changed altitudes between 3km to 500m, but spent most of its time around 1km. At this height, the pollutant concentrations can be affected significantly by surface emissions. Figure 9 shows that the simulations with time-fixed and profile BCs tend to overestimate CO and O_3 for this flight segment, while the simulation with original time-varied BCs yields reasonable results. It should be noted that these three simulations show similar variations, and the predicted differences are mainly due to their different background concentrations. The simulation with time-fixed BCs yielded about 40 ppbv higher CO and 30 ppbv higher O_3 concentrations than that with original BCs, and the simulation with profile BCs are about 50 and 40 ppbv higher for CO and O_3, respectively. The differences are relatively small at 23 UTC compared with the segment from 24 to 25 UTC. Figure 10 shows that the flight location at 23 UTC is downwind of flight segment at 24-25 UTC. So the difference from the lateral boundary conditions was diluted after the transport. Figure 10 also shows the wind field and simulated concentrations in the model's 1km layer. For this flight segment, the airmass mainly came from south and southwest direction. The 24-25 UTC segment encountered relatively clean airmass from the ocean in the southeast boundary of this domain, and the simulation with original BCs predicted CO < 80 ppbv and O_3 < 30 ppbv near this boundary. For the same area, the

simulation with time-fixed BCs showed CO > 100 ppbv and O_3 > 50 ppbv, and the profile-BCs case had CO > 130 ppbv and O_3 > 65 ppbv (Figure 9). This event analysis clearly shows the model's sensitivity to south inflow boundary conditions. During this period, this domain's west boundary was also an inflow boundary. For the area near the domain's west boundary, the simulation with original BCs predicted up to 100 ppbv higher CO and 60 ppbv higher O_3 concentration than the simulations with time-fixed and profile BCs. During this event, the difference between original BCs and profile BCs is greater than that between original BCs and time-fixed BCs, since profile BCs includes less information of variance.

4.2 WP-3 flight on August 6

Figure 11 shows the comparison between observations and predictions for a WP-3 flight segment on August 6, a region from Ohio River Valley to New Hampshire (Figure 12). In this event, the simulation with the time-mean and profile BCs tended to overpredict O_3 and NO_z (NO_y - NO_x). The O_3 overprediction is related to NO_z overprediction for most of this flight segment. Trainer et al. (1993) found that O_3 was highly correlated with NO_z downwind of pollution plumes, and the ratio of $\Delta O_3/\Delta NO_z$ could represent the upper limit of the ozone production efficiency (OPE) per unit NO_x in the photochemical process. In this event, these three simulations have the same emissions, and they also tend to have similar OPE. Figure 12 shows that the north boundary brought the inflows of NO_z and O_3, which was relatively clean. The NO_z differences among these simulations could be up to 2 ppbv near the north boundary, and the corresponding O_3 differences are up to 20 ppbv. These differences narrowed when the airmass reached further inside the domain, but they could still affect the models' predictions. As shown by Figure 11, these differences among the simulations with original, time-mean and profile BCs reached 10 ppbv for O_3 and 1 ppbv for NO_z along with this flight path. The simulation with time-mean BCs is similar to that with profile BCs. It should be noted that there are also positive differences of O_3 and NO_z between the simulations with original BCs and time-fixed BCs (Figure 12B, 12E), especially downwind of New York and Boston, which is correlated with their CO differences (not shown) brought by the northeast inflow. Near the western inflow

boundary, the simulated NO_z with original BCs is higher than those with time-mean and profile BCs (Figure 12E, 12F), while the O_3 differences do not show this pattern (Figure 12B, 12C). Since the west boundary is located inland where pollutant emissions are relatively strong, fresh NO_x emissions sometimes does not benefit O_3 production, but instead titrates O_3. So it is reasonable that O_3 difference is not correlated with NO_z there. On the other hand, the simulated O_3 difference shows good correlation with corresponding NO_z differences farther downwind of pollutant sources or in relatively clean areas, such as over the ocean.

These results show that the model's sensitivity to the BCs varies from location to location. The locations near the inflow boundaries have the highest sensitivity to the variation of BCs. This event and the flight on July 31 show that clean areas without strong emission, such as ocean, are more sensitive to the BCs than the polluted areas. In another word, the difference of BCs becomes narrowed faster over polluted areas than that over clean areas.

5. Overall Evaluation

Through the scenario analyses, we can see the regional model's dependence on lateral and top boundary conditions. However, these analyses are based on event cases, and did not give an overall picture. Here we analyze the input of the model performance under different BCs using statistical and other methods.

5.1 Statistical Results due to Different Global BCs Compared to Aircraft Measurements

Table 1 shows the correlations between the DC-8 observations and the simulations with boundary conditions from the three global models. The DC-8 flight paths covered nearly the whole USA during the ICARTT period, with altitude ranging from 200m to 12km. Figure 13 shows the NASA DC-8 and NOAA WP-3 flight paths during this period. The

simulation with RAQMS BCs produced the overall highest correlation coefficient (R) and the best correlation slope with the observed O_3, but its mean O_3 concentration is about 8 ppbv higher than the measurements. The 60km simulation with MOZART-GFDL BCs yielded the O_3 mean concentration with the lowest bias. The simulation driven by MOZART-NCAR BCs tended to underestimate O_3, especially in the higher altitudes, and produced the lowest regression slope (0.43). The simulation with MOZART-GFDL BCs overestimated the mean CO by 20 ppbv, but its correlation slope (1.87) was high as it has higher mean background CO. The simulation with RAQMS BCs produced the CO mean concentration with the lowest bias, but with high CO correlation slope. MOZART-NCAR had the best CO correlation slope. All of the simulations yielded similar CO correlation coefficients. HNO_3 is one product of the NO_x photochemical reactions, and its production rate depends on ambient NO_x, O_3 and OH concentrations. The simulation with RAQMS BCs had the lowest bias of the mean HNO_3, and the other two simulations tended to overpredict HNO_3. Table 1 shows that all the simulations tended to overestimate the OH concentrations, and the simulation with MOZART-NCAR BCs produced the highest correlation coefficients. The general feature for HO_2 predictions are similar to those for OH, but were better in terms of mean concentration and correlations.

A similar comparison for the NOAA WP-3 flights is shown in Table 2. The WP-3 aircraft mainly flew over the northeastern USA with altitudes ranging from 200m to 7km, including many research flights studying urban plumes. Table 2 shows that the 60km simulation with RAQMS BCs has the best overall prediction for O_3 among these 60km simulations, evaluated in terms of mean value, slope and correlation coefficient. That simulation also yielded the highest R (0.67) for CO comparison, but its mean CO concentration was 13 ppbv lower than the observation. The CO prediction with MOZART-NCAR BCs has the lowest mean bias, and the MOZART-GFDL tended to overpredict CO as shown by the slope of 1.62. These three simulations differ little in their predictions of NO_z, SO_2 and fine sulfate, implying that regional and local emissions played a more important role on these emission-related species than the forcing from boundaries over the northeastern USA. In general, the differences among these three simulations for WP-3 flights are smaller than those for DC-8 flights as the DC-8 flew

over broader regions and at higher altitudes, and had more flight paths near the domain's lateral and top boundaries. For long-lived high-concentration species, like CO, the influence due to different boundary conditions can be shown throughout the domain. During the ICARTT period, the most significant CO inflow was the forest fire plumes from Alaska and Canada, which entered the STEM 60km domain from its north lateral boundary. The most significant O_3 inflow occurred near the domain top from the stratosphere, which affected DC-8 flights more than WP-3 flights. For most short-lived emitted species, the influence of BCs is relatively weak as the strong emissions within the domain show greater impact.

Figure 14 shows the CO and O_3 mean vertical profiles and standard deviations for these DC-8 and WP-3 flights. Both aircraft measurements show that the biggest CO standard deviation appears in altitudes from 2.5 to 4km, which reflect the turbulent lofting within the planetary boundary layer (PBL), convection and forest fire plumes. However, none of the simulations captured the magnitude of the observed variation. The simulation with MOZART-GFDL BCs tended to overpredict the mean CO below 6km for the WP-3 flights, and below 8km for DC-8 flights, while the simulation driven by MOZART-NCAR BCs underestimated CO above 4km (Figure 14A, 14C). For O_3 prediction, the three simulations have similar behavior below 1km. Above 4km, the simulation with MOZART-NCAR BCs underestimated the O_3 mean concentration, and RAQMS BCs resulted in the O_3 overepredictions above 6km (Figure 14B, 14D). The DC-8 observations show the biggest O_3 mean concentration and standard deviation near the top of troposphere (Figure 14B), where the simulation with MOZART-GFDL BCs best captured the mean O_3 concentration, and MOZART-NCAR tended to underestimate O_3 while RAQMS overestimated O_3 in this region. Figure 14B also shows that the MOZART-NCAR model underestimated the O_3 deviation in this top altitude, and the other two global models resulted in larger variations. All observations and models found that the minimum O_3 standard deviation was in the altitude 3-5 km. The small O_3 deviation above 6km for WP-3 flights (Figure 14D) is mainly due to its relatively few data points.

5.2 Statistical Results of Model's Sensitivity to Temporal and Spatial Variations of Boundary Conditions

We also analyzed the difference among the simulations with original time-varied BCs, time-mean BCs and profile BCs in the 60km and 12km domain. Table 3 is similar to Table 1 but for the 60km simulations with original MOZART-NCAR, time-mean and profile boundary conditions. It is evident that the 60km simulation with the original MOZART-NCAR BCs has a better correlation slope and coefficient (R) than those with averaged BCs for O_3. It is reasonable because temporal and spatial averaging remove O_3 variation information from the top and lateral boundaries. However, the mean O_3 concentrations differ little, and the time-varied BCs do not show any advantage on predicting the mean O_3 values. Their difference on CO prediction is even smaller because original inflow BCs for the CO do not have variations as strong as its stratospheric O_3, except for special events, such as forest fire plumes. Comparison for HNO_3 shows similar trends. The time-varied BCs did not show better results for predicting short-lived species, like OH and HO_2.

The corresponding results for 12km simulations compared to NOAA WP-3 observation are shown in Table 4. It should be noted that the 12km domain covered most, but not all of the WP-3 flights. However, these statistical results do show the advantage of higher resolution as the 12km simulation (Table 4) yielded better correlation coefficients than the 60km simulation (Table 2) for CO, O_3 and SO_2. The difference among the three BCs is more significant in the 12km simulation than in the 60km simulation. The simulation with original BCs is better than the simulations with time-mean and profile BCs for most species. The advantage of time-varied BCs is shown not only on CO and O_3, but also on emitted and relatively short-lived species, like SO_2 and propane. Acetone is a long-lived emitted species, which has strong emissions in the continental USA, and the time-varied BCs also has advantage on predicting this species. For the 12km domain, the major inflow forcing comes from its upwind areas, including U.S. Midwest and California, with high pollutant emissions. For instance, Chicago is one of major regional contributors to inflow pollutants in the 12km domain. The weather-driven airflow could bring the strong

and distinct upwind Chicago signals to this domain. After temporal and spatial averaging, this signal becomes relatively uniform. In the contrast, the 60km domain's inflow boundary is located over relatively clean areas, like the eastern Pacific and Canada, where the natural pollutant signals becomes relatively uniform after long-range transport and dynamical diffusion (except for some special events). So the 60km domain is not as sensitive to the removal of temporal and spatial variations on BCs as the nested 12km domain. In the 12km domain, the time-varied BCs also yield better results for secondary species, such as PAN and O_3.

To further investigate the model's sensitivity to temporal and spatial variations of boundary conditions and its dependence on location and scale, we compare the CO vertical profiles in model gridpoints 5 grid cells from the west, east, south and north boundaries of the 60 km simulations in Figure 15. The west boundary is mainly located along the US west coast, where California emissions are a strong contributor to CO. So, all the three simulations with original, time-mean and profile BCs show similar strong CO deviations in low altitudes, and this deviation decreases with altitude. The biggest difference among these simulations is the CO standard deviation above 9km near the west inflow boundary, where the simulation with original BCs shows much greater variation than the others, though they have similar mean concentration. During the summertime, Asian airmass inflow still exists, but not as strong as that during springtime. The CO standard deviation in the simulation with the original BCs is about 5 ppbv at altitudes above 9km. The other two simulations remove the temporal and both temporal and spatial variations from the lateral boundary, and so their variations become much weaker. The east boundary is the prevailing outflow boundary of this 60km domain, but Figure 15B still shows that the simulation with original BCs yielded greater standard deviations than the simulations with averaged BCs, especially in the high altitudes. Near the south boundary, the simulations have the minimum differences on their standard deviations, even at high altitudes. Near the north boundary along the USA-Canada border, these simulations make the biggest difference on the CO standard deviation. The original BCs contain strong and highly time-varied CO inflows, including forest fires and Asian plumes. The simulation with the original MOZART-NCAR BCs shows strong CO

variation in the altitudes from 6km to 9km. All simulations with averaged BCs missed this feature, which even produced mean concentration biases (Figure 15D). Figure 16 shows the corresponding comparison for the 12km domain covering the northeastern USA. In this domain, the prevailing inflow boundaries are also located in the west and north. The CO variability in the 12km domain is higher than that in the 60km domain, reflecting the difference in regional resolution. The only exception is for the south boundary (Figure 16C), which had weak variations, and all three simulations yielded similar mean CO profiles in this region. Near all the other boundaries, the simulation with original BCs has not only larger CO variations than the two simulations with averaged BCs, but also has a different mean CO profile. Figure 16A shows that the three simulations show similar CO standard deviations below 2km, due to their same emissions, but the mean CO profiles differ significantly, while the simulation with the original BCs yielded the higher CO mean concentration. This simulation also has the higher CO variations in the east and north boundaries at low altitudes. Near all the four boundaries, the simulation with original BCs has higher CO variation in high altitudes than the other two, which is similar to the case in the 60km domain. The CO variation difference among these simulations in low altitudes reflects that the simulations with averaged BCs fail to represent the CO emission and transport from polluted upwind areas, which could immediately adjoin to the model domain.

5.3 The Contribution of Lateral Boundary Conditions Represented by Influence Functions.

The above discussion shows that the sensitivity at a given receptor to boundary conditions depends on domain characteristics, such as wind field, emissions and strength of boundary flux. To more quantitatively describe these characteristics, we introduce an influence function as

$$C_i(x,y,z) = \sum_{n=0}^{N-1} \lambda_i(x,y,z,t) \qquad (1)$$

where i is the chemical species index, N is the total number of time steps, and $\lambda_i(x,y,z,t)$ is the adjoint variable calculated from STEM adjoint model (Sandu et al., 2005; Chai et

al., 2006). After choosing a target species and target region at certain time, $\lambda_i(x,y,z,t)$ is the sensitivity function of the target with respect to $C_i(x,y,z,t)$. Thus, the time-integrated sensitivity, i.e. the influence function $C_i(x,y,z)$, provides the information on how the model predictions are affected by the boundary conditions.. Figure 17 shows the 5-day integrated (July 19-24) $C_{co}(x,y,z)$ (CO as target species) distribution with MOZART-NCAR boundary condition in our 60km domain for the target grid box shown in Figure 17A. The target box has vertical extent from 1 to 4km above ground. Figure 17A illustrates the vertically integrated influence of CO on CO. The emission sources from Texas have a strong influence on the target area during this period. In addition to this emission influence, the north boundary condition is the major influencing factor, which extends an area of the influence from northwest boundary to the target area. Figure 17B shows the vertical extent of the CO-on-CO influence function along the cross-section of the north boundary, and we can see that the high influence came from altitudes 1-3 km, and these high CO levels were due to forest fires in Canada and Alaska. Figure 17C shows mean profile of this influence function and its spatial standard deviation along the 4 lateral boundaries during this 5-day period. In this scenario, the north boundary had the biggest influence on this domain with peak value in 2km, while south boundary's influence existed mainly below 3km, and west boundary showed influence above 3km due to the CO pollutant from Asia. The east boundary has low influence as it is an outflow boundary. The O_3-on-O_3 influence function is similar to CO-on-CO but its peak values appear at higher altitudes: 3km (Figure 17D), which reflected some upper-layer ozone contribution. Figure 17E shows the chemical contribution of CO to O_3 in this influence function. In this case, CO mainly contributes to O_3 photochemical production. The west-boundary inflow of CO shows the highest O_3 production efficiency, and the north boundary has the lowest one. This chemical conversion mainly depends on which kinds of airmass mix with the boundary-inflow CO. Near west and south inflow boundaries, there are abundant NO_x emissions that benefit CO contribution to O_3, while the region near the north boundary (north Dakota et al.) are relatively clean.

6. Conclusion

In this study, we test the influence of boundary conditions from 3 global models on regional chemical transport model, STEM-2K3. Our study shows that STEM's performance is sensitive to BCs for relatively long-lived transported species, such as CO and O_3. The most important advantage of using global model as BCs is that these BCs can bring time-varied external signal to the regional domain, and reflect certain event information, such as biomass burning, stratospheric intrusion, and Asian airmass inflow. Due to the different schemes, configurations, meteorology and emissions, the three global models, MOZART-NCAR, MOZART-GFDL and RAQMS show different performance during the ICARTT period. In generally, RAQMS has the highest O_3 concentration, especially near top of troposphere, where MOZART-NCAR has the lowest O_3 among them. Although they differ so significantly, it is interesting that none of these models has systematical bias compared to aircraft observed O_3 (except in the upper troposphere), and their performances varied from case to case. As shown by the case studies, the simulation with MOZART-NCAR BCs yields better O_3 result in DC-8 flight 8 on July 15, and the simulation with RAQMS BC successfully capture the O_3 peak value in WP-3 flight on July 28. Among these models, MOZART-NCAR has the lowest CO and O_3 predictions, and MOZART-GFDL has the highest mean CO concentration, while RAQMS has the highest O_3 top boundary conditions. It should be noted that these models' differences on other species could be greater. In this study, we just focus on O_3 and CO as an example. STEM's sensitivity to time-varied BCs is also varied from case to case. In general, the regional model is very sensitive to BCs over the grids near inflow boundaries, such as high altitudes and northern inflow boundary. The model's sensitivity to BCs also depends on the strength of regional and local emissions. If local emission is overwhelmingly strong, such as in urban sites, the model prediction near ground becomes less sensitive to variation of BCs, but to its background magnitude.

Our study about regional model's sensitivity to the temporal and spatial variation of BCs tells a similar story, but in two scales. Our analysis indicates that even if none of the global boundary conditions is perfect, they can still drive the regional model to yield better results than that with pre-defined profile BCs, especially in correlations with

aircraft measurements, since global models can bring time-varied external signals. Boundary conditions are more important to small domain than to big domain. Our sensitivity study shows the model has higher dependence on lateral boundaries in 12km domain than that in 60km domain, as the 12km domain has more distinguished inflow signal due to its locations. In the 12km domain, the BCs in low altitudes could be more important as the high concentrated pollutant inflow exists in lower levels, and even some short-lived species, like SO_2, could be affected. This analysis shows that small-scale high-resolution predictions are more sensitive to boundary conditions and their variations than the large-scale prediction.

From this study, we can expect to get better prediction by ensemble of the global boundary conditions since each of them has advantage from case to case. During the summertime, continental-scale regional prediction over ground is not very sensitive to lateral boundary conditions since these BCs are not highly varied, but these BCs are still important for the prediction in elevated levels. For finer scale simulation, like urban air quality prediction, the time-varied BCs that includes external inflow is very necessary and predefined BCs can not be reasonably used in this case.

Reference:

Carter, W., 2000, Documentation of the SAPRC-99 chemical mechanism for voc reactivity assessment, Final Report to California Air Resources Board Contract No. 92-329, University of California-Riverside, May 8.

Chai, T. G. R. Carmichael, A.Sandu, Y. Tang and D. N. Daescu, 2006, Chemical data assimilation of transport and chemical evolution over the Pacific (TRACE-P) aircraft measurements, *J. Geophys. Res., 111, D02301, doi: 10.1029/2005JD005883.*

Chen, K.S., Y. T. Ho, C. H. Lai, Y.-M. Chou, 2003, Photochemical modeling and analysis of meteorological parameters during ozone episodes in Kaohsiung, Taiwan, *Atmos. Environ.*, 37, 1811-1823.

Geron, C. D., A. B. Guenther, and T. E. Pierce, 1994, An improved model for estimating emissions of volatile organic-compounds from forests in the eastern united-states. *J. Geophys. Res.,* 99 (D6): 12773-12791.

Gong, S. L., 2003, A parameterization of sea-salt aerosol source function for sub- and super-micron particles, *Global Biogeochem. Cycles*, 17(4), 1097, doi:10.1029/2003GB002079.

Grell, G. A., J. Dudhia and D. R. Stauffer, 1994, A description of the fifth-generation Penn State/NCAR mesoscale model (MM5). NCAR Technical Note, NCAR/TN-398+STR, 117 pp.

Hong, S.-Y., and H.-L. Pan, 1996, Nonlocal boundary layer vertical diffusion in a medium-range forecast model. *Mon. Wea. Rev., 124, 2322-2339*.

McLinden, C.A., S.C. Olsen, B. Hannegan, O. Wild, and M. J. Prather， 2000, Stratospheric ozone in 3-D models: A simple chemistry and the cross-tropopause flux, *J. Geophys. Res., 105(D11), 14,653-14,665.*

Olivier, J. G. J. and J. J. M. Berdowski, 2001, Global emissions sources and sinks. In: Berdowski, J., Guicherit, R. and B.J. Heij (eds.) "The Climate System", pp. 33-78. A.A. Balkema Publishers/Swets & Zeitlinger Publishers, Lisse, The Netherlands. ISBN 90 5809 255 0.

Pfister, G., P. G. Hess, L. K. Emmons, J.-F. Lamarque, C. Wiedinmyer, D. P. Edwards, G. Pétron, J. C. Gille, and G. W. Sachse, 2005, Quantifying CO emissions from the 2004 Alaskan wildfires using MOPITT CO data, *Geophys. Res. Lett.*, *32*, L11809, doi:10.1029/2005GL022995.

Pickering, K. E., Y. Wang, W.-K. Tao, C. Price, and J.-F. Müller, 1998, Vertical distributions of lightining NOx for use in regional and global chemical transport models, *J. Geophys. Res., 103(D23), 31203-31216.*

Pierce, R. B., et al., 2003, Regional Air Quality Modeling System (RAQMS) predictions of the tropospheric ozone budget over east Asia, J. Geophys. Res., 108(D21), 8825, doi:10.1029/2002JD003176.

Price, C. and J. Penner, 1997, NOx from lightning 1: global distribution based on lightning physics. *J. Geophys. Res., 102(D5), 5929-5941.*

Sandu, A., D. Daescu, G. R. Carmichael and T. Chai, 2005, Adjoint sensitivity analysis of regional air quality models, *J. Comput. Phys., 204(1), 222-252.*

Tang, Y., G. R. Carmichael, I. Uno, J.-H. Woo, G. Kurata, B. Lefer, R. E. Shetter, H. Huang, B. E. Anderson, M. A. Avery, A. D. Clarke and D. R. Blake, 2003a,

Impacts of aerosols and clouds on photolysis frequencies and photochemistry during TRACE-P, part II: three-dimensional study using a regional chemical transport model, *J. Geophys. Res., 10.1029/2002JD003100*.

Tang, Y., G. R. Carmichael, J.-H. Woo, N. Thongboonchoo, G. Kurata, I. Uno, D. G. Streets, D. R. Blake, R. J. Weber, R. W. Talbot, Y. Kondo and H. B. Singh, 2003b, The Influences of Biomass Burning during TRACE-P Experiment Identified by the Regional Chemical Transport Model, *J. Geophys. Res., 108(D21), 8824, doi:10.1029/2002JD003110*.

Tang, Y., G. R. Carmichael, J. H. Seinfeld, D. Dabdub, Rodney J. Weber, B. Huebert, A. D. Clarke, S. A. Guazzotti, D. A. Sodeman, K. A. Prather, I. Uno, J.-H. Woo, D. G. Streets, P. K. Quinn, J. E. Johnson, C.-H. Song, A. Sandu**,** R. W. Talbot and J. E. Dibb, 2004, Three-dimensional simulations of inorganic aerosol distributions in East Asia during spring 2001, *J. Geophys. Res., 109, D19S23, doi:10.1029/2003JD004201*.

Trainer, M., D. D. Parrish, M. P. Buhr, R. B. Norton, F. C. Fehsenfeld, K. G. Anlauf, J. W. Bottenheim, Y. Z. Tang, H. A. Wiebe, J. M. Roberts, R. L. Tanner, L. Newman, V. C. Bowersox, J. F. Meagher, K. J. Olszyna, M. O. Rodgers, T. Wang, H. Berresheim, K. L. Demerjian and U. K. Roychowdhury, 1993, Correlation of ozone with NOy in photochemical aged air. J. Geophy. Res., 98(D2), 2917-2925.

Winner, D. A., G. R. Cass, and R. A. Harley, 1995, Effect of alternative boundary conditions on predicted ozone control strategy: a case study in Los Angeles area. *Atmos. Environ.*, 29(33), 3451-3464.

Table 1. The statistic result of 60km simulations with the three boundary conditions compared with the observations in NASA DC-8 flights 3-20. The correlation slope and coefficient (R) are presented in model (y) versus observation (x).

		60km Simulated with MOZART-NCAR BCs			60km Simulated with MOZART-GFDL BCs			60km Simulated with RAQMS BCs		
Species	**Observed Mean**	**Simulated Mean**	**Slope**	**R**	**Simulated Mean**	**Slope**	**R**	**Simulated Mean**	**Slope**	**R**
O_3 (ppbv)	67.0	61.4	0.43	0.57	63.0	0.58	0.58	75.54	0.87	0.60
CO (ppbv)	112.8	105.2	1.12	0.67	134.4	1.87	0.67	113.6	1.53	0.71
HNO_3 (ppbv)	0.55	0.69	1.18	0.62	0.67	1.18	0.60	0.54	1.15	0.61
OH (pptv)	0.22	0.36	0.92	0.43	0.31	0.81	0.41	0.33	0.83	0.42
HO_2 (pptv)	13.1	15.0	1.04	0.54	15.5	1.06	0.56	15.5	1.07	0.54

Table 2. The statistic result of 60km simulations with the three boundary conditions compared with the observations in all NOAA WP-3 research flights. The correlation slope and coefficient (R) are presented in model (y) versus observation (x).

		60km Simulated with MOZART-NCAR BCs			60km Simulated with MOZART-GFDL BCs			60km Simulated with RAQMS BCs		
Species	**Observed Mean**	**Simulated Mean**	**Slope**	**R**	**Simulated Mean**	**Slope**	**R**	**Simulated Mean**	**Slope**	**R**
O_3 (ppbv)	59.6	57.4	1.07	0.61	57.2	1.19	0.57	59.4	1.09	0.61
CO (ppbv)	144.5	148.7	0.98	0.55	189.9	1.62	0.55	157.6	1.18	0.67
NO_z (ppbv)	2.87	3.20	1.26	0.43	3.14	1.33	0.44	3.01	1.31	0.45
SO_2 (ppbv)	1.51	2.06	0.75	0.61	2.07	0.78	0.60	2.06	0.78	0.60
Fine Sulfate ($\mu g/std\ m^3$)	4.17	5.53	0.80	0.57	5.37	0.80	0.58	5.66	0.81	0.58

Table 3. The statistic results of 60km simulations with the original MOZART-NCAR, time-mean and profile boundary conditions compared with the observations in NASA DC-8 flights 3-20. The correlation slope and coefficient (R) are presented in model (y) versus observation (x).

		60km Simulated with MOZART-NCAR BCs			60km Simulated with Time-Mean BCs			60km Simulated with Profile BCs		
Species	**Observed Mean**	**Simulated Mean**	**Slope**	**R**	**Simulated Mean**	**Slope**	**R**	**Simulated Mean**	**Slope**	**R**
O_3 (ppbv)	67.0	61.4	0.43	0.57	63.4	0.37	0.51	62.9	0.35	0.49
CO (ppbv)	112.8	105.2	1.12	0.67	106.1	1.06	0.66	105.5	1.01	0.66
HNO_3 (ppbv)	0.55	0.69	1.18	0.62	0.56	1.09	0.61	0.56	1.10	0.61
OH (pptv)	0.22	0.36	0.92	0.43	0.30	0.78	0.50	0.30	0.77	0.49
HO_2 (pptv)	13.1	15.0	1.04	0.54	15.5	0.93	0.55	15.5	0.94	0.55

Table 4. The statistic result of 12km simulations with the original, time-mean and profile boundary conditions compared with the observations in all NOAA WP-3 research flights. The correlation slope and coefficient (R) are presented in model (y) versus observation (x).

		12km Simulated with Original BCs			12km Simulated with Time-Mean BCs			12km Simulated with Profile BCs		
Species	**Observed Mean**	**Simulated Mean**	**Slope**	**R**	**Simulated Mean**	**Slope**	**R**	**Simulated Mean**	**Slope**	**R**
O_3 (ppbv)	59.6	61.8	1.13	0.65	63.3	0.57	0.51	63.7	0.55	0.48
CO (ppbv)	144.5	153.6	1.07	0.61	151.2	0.76	0.57	151.1	0.76	0.56
PAN (ppbv)	0.42	0.78	0.71	0.47	0.73	0.48	0.41	0.72	0.50	0.44
SO_2 (ppbv)	1.51	2.64	0.78	0.63	2.62	0.76	0.62	2.62	0.77	0.62
Propane (ppbv)	0.38	0.31	0.67	0.64	0.30	0.61	0.63	0.30	0.60	0.63
Acetone (ppbv)	1.91	1.03	0.60	0.69	1.06	0.44	0.60	1.06	0.44	0.58

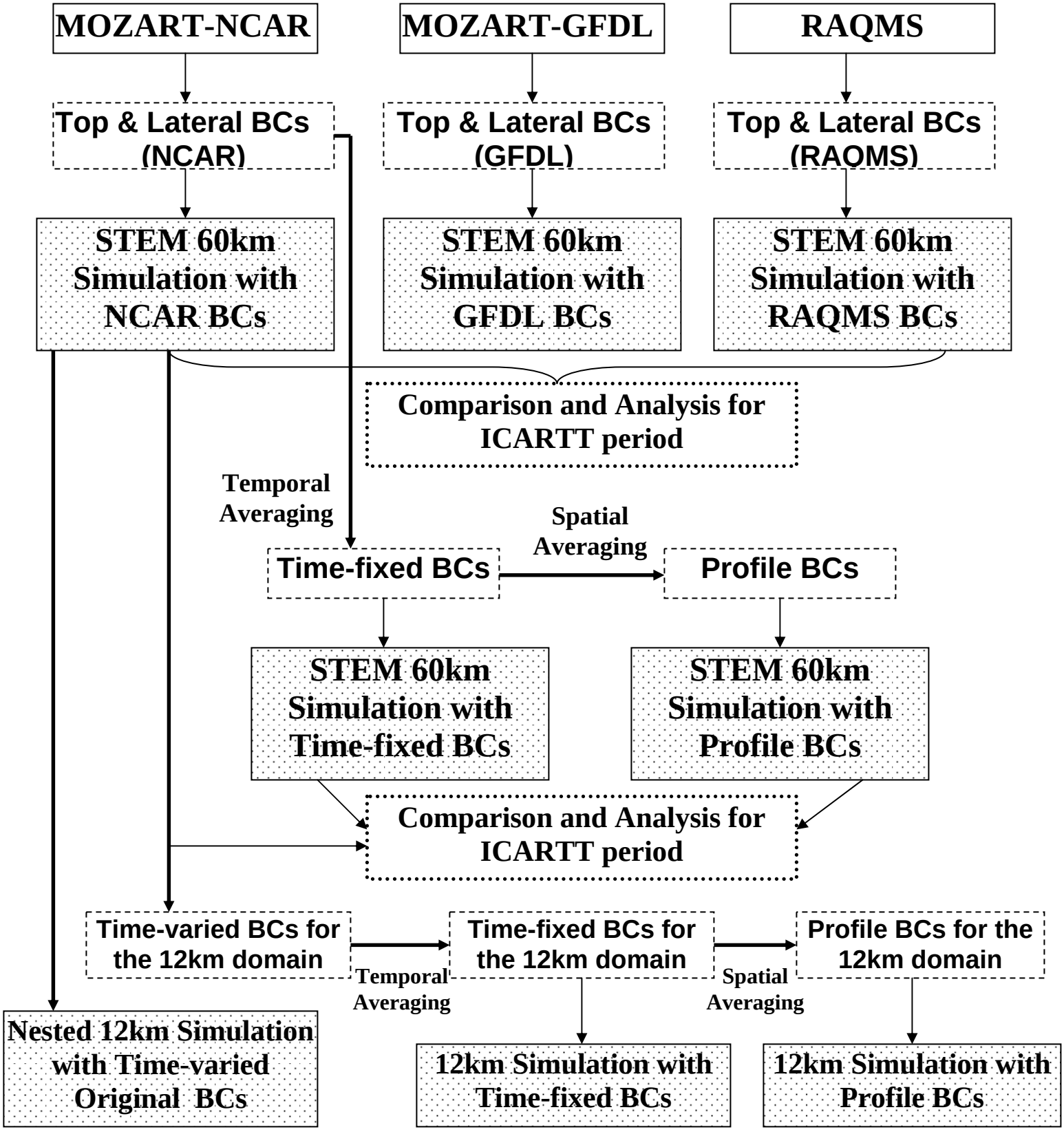

Figure 1. Comparison and Analysis Framework

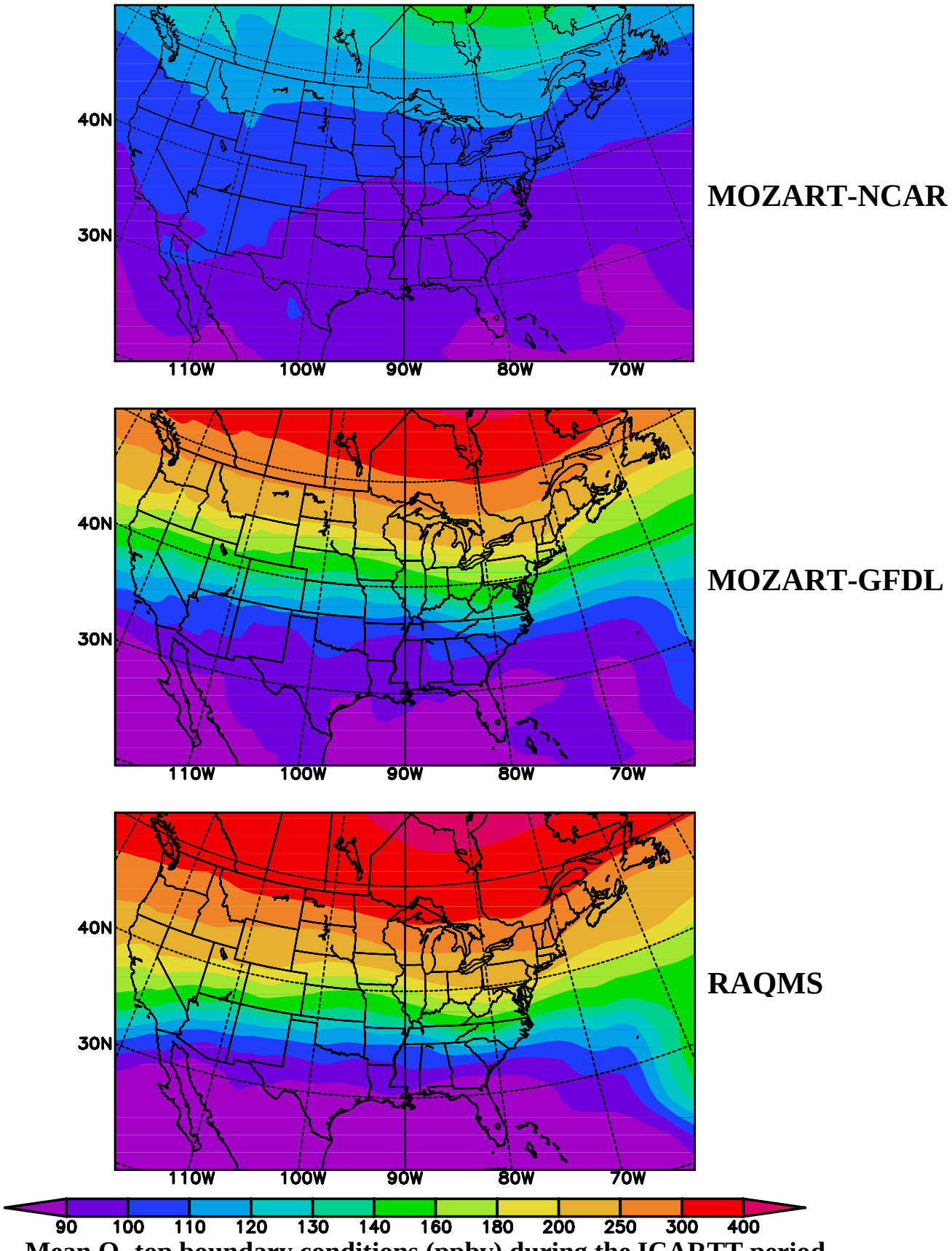

Figure 2. Period-mean O_3 top boundary conditions from 3 global models.

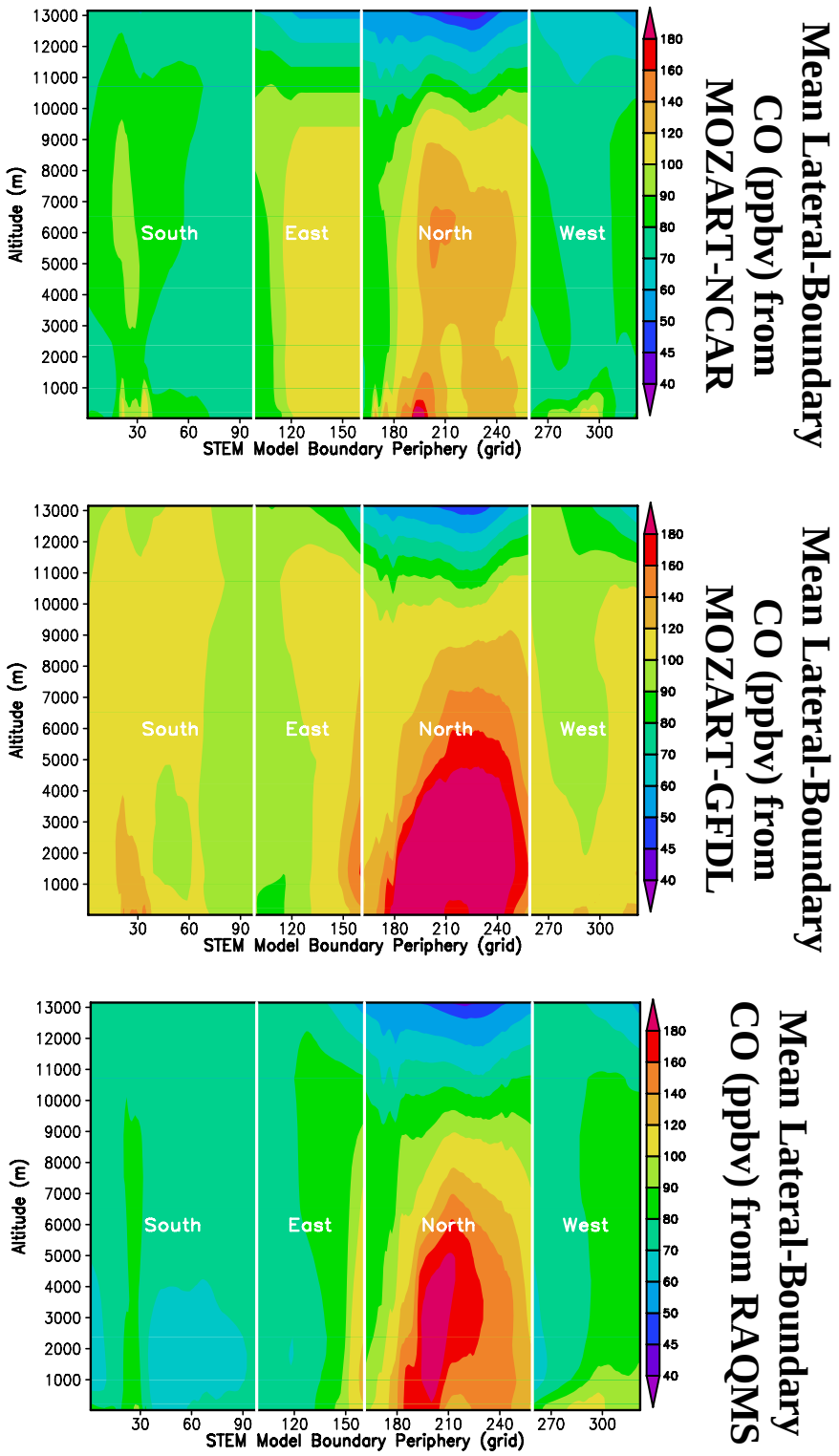

Figure 3. Period-mean CO lateral boundary conditions from 3 global models, along the STEM's boundary periphery in grid (60km) starting from the southwest corner of the STEM 60km domain shown in Figure 1.

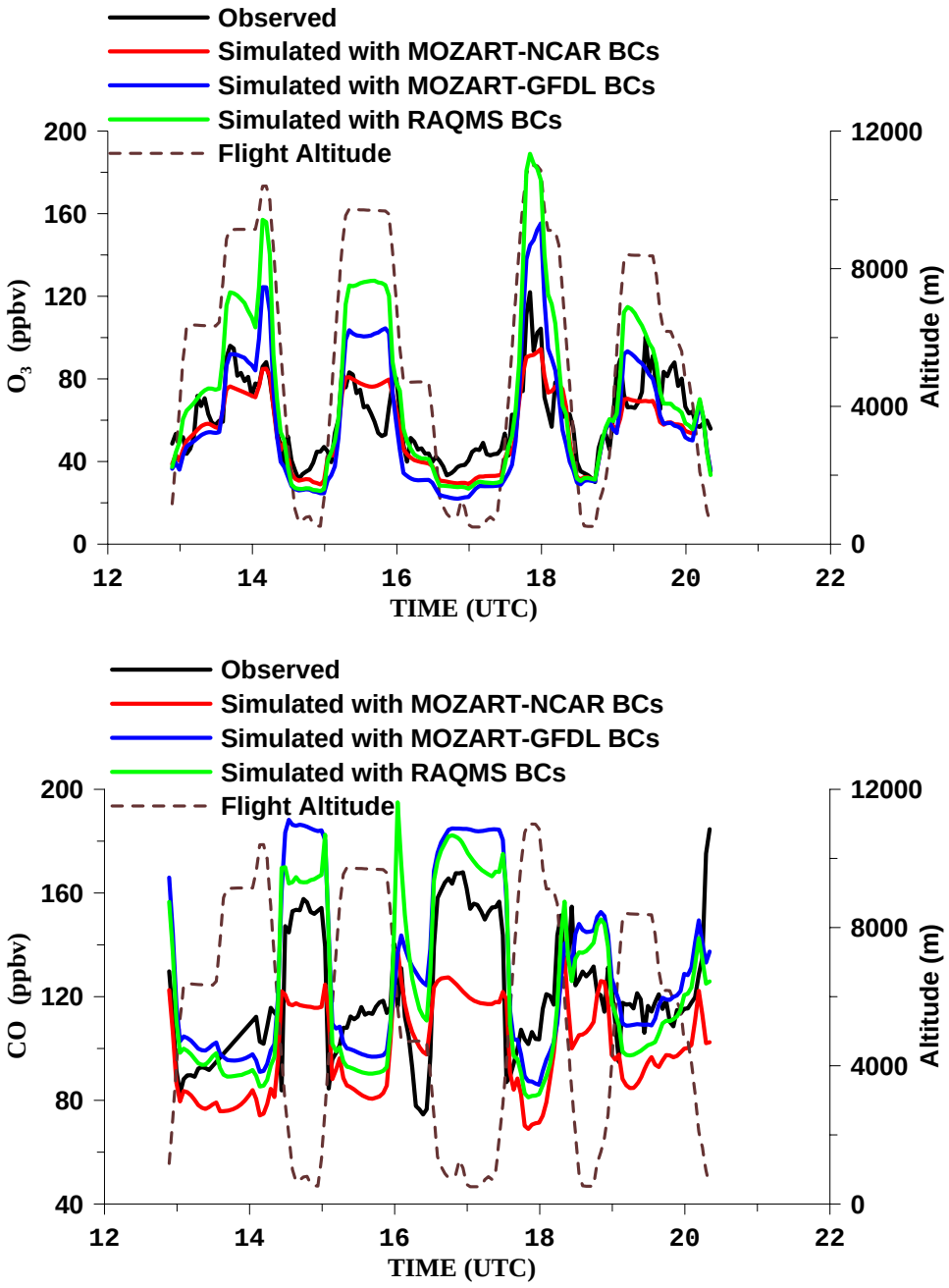

Figure 4. Observed and Simulated O_3 and CO concentrations for the DC-8 flight 8 on 07/15/2004

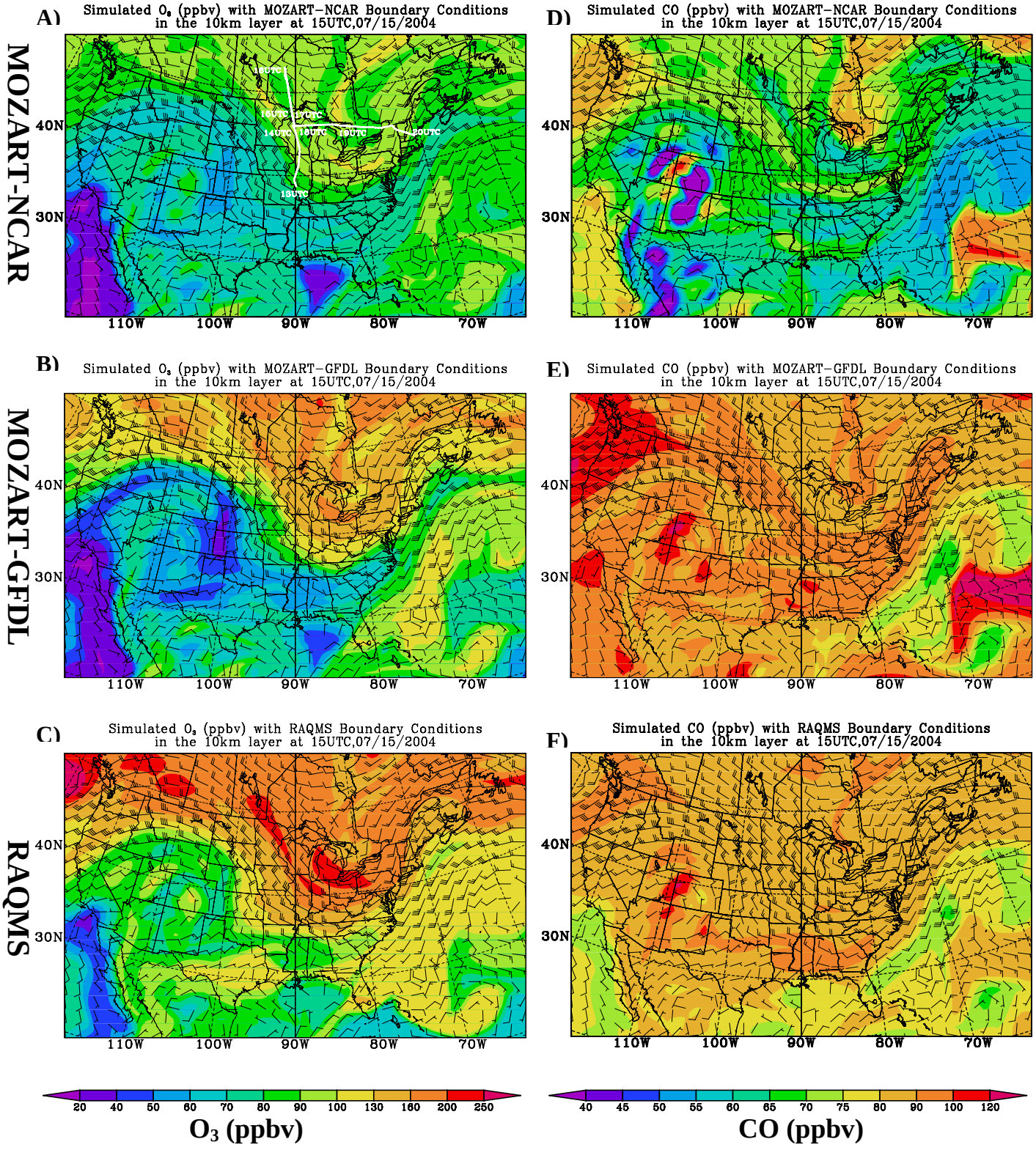

Figure 5. STEM 60km simulated O_3 and CO concentrations in the 10km layer with boundary conditions from the three global models for DC-8 flight 8 on July 15 (plot A shows the flight path).

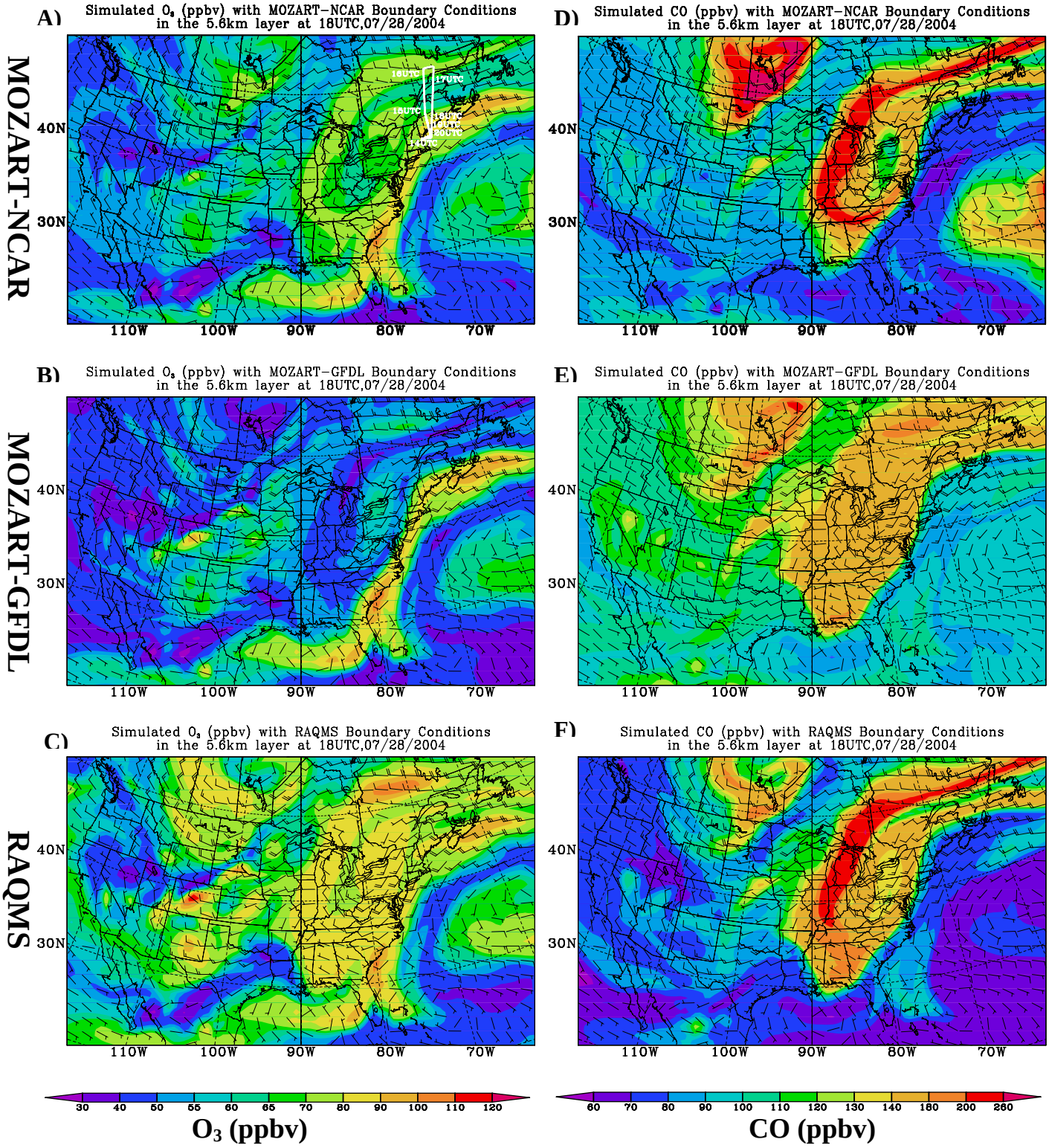

Figure 6. STEM 60km simulated O_3 and CO concentrations in the 5.6km layer with boundary conditions from the three global models for WP-3 flight 12 on July 28 (plot A shows the flight path).

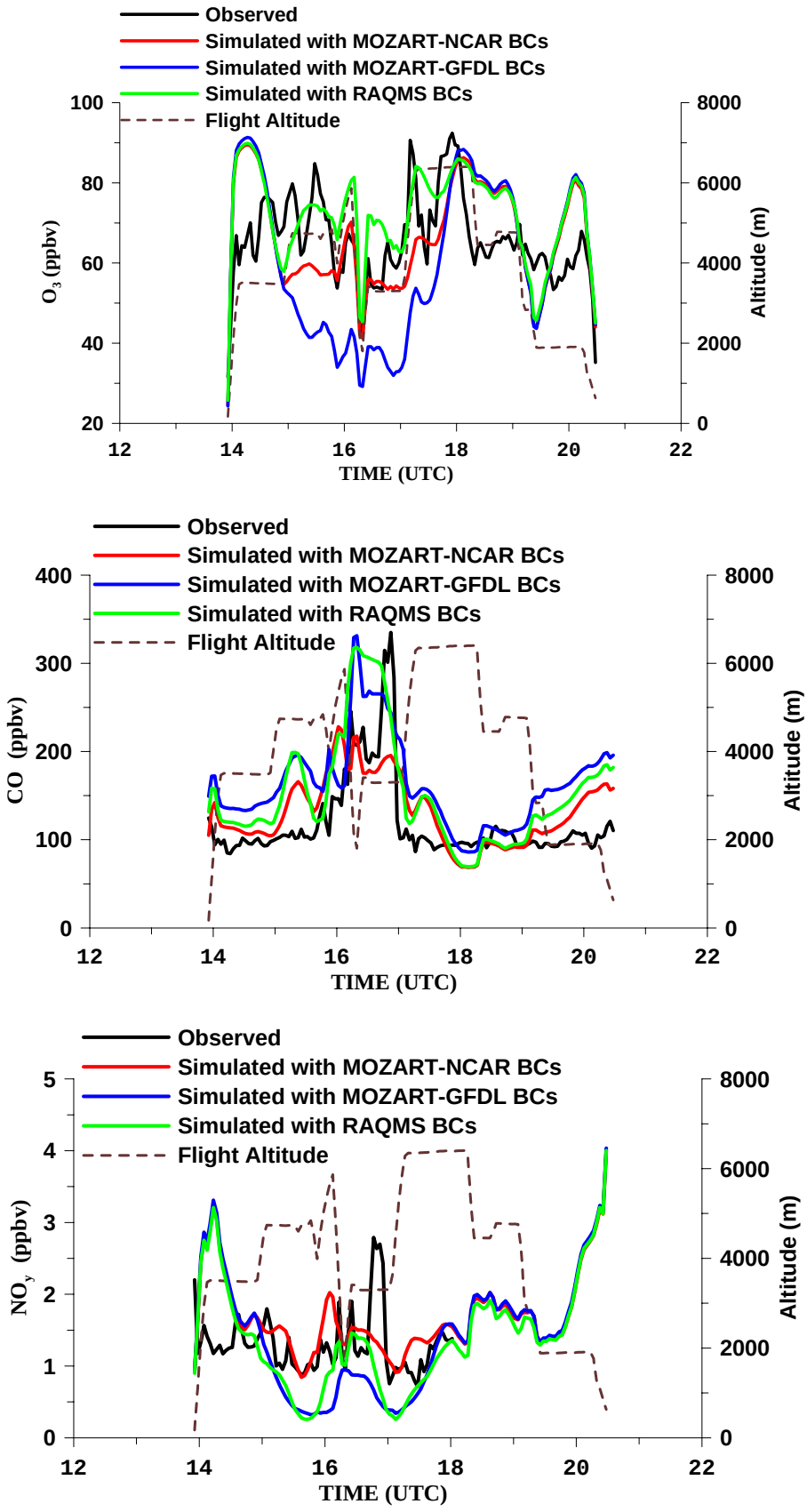

Figure 7. Observed and simulated O_3, CO, and NO_y concentrations for the WP-3 flight 12 on 07/28/2004

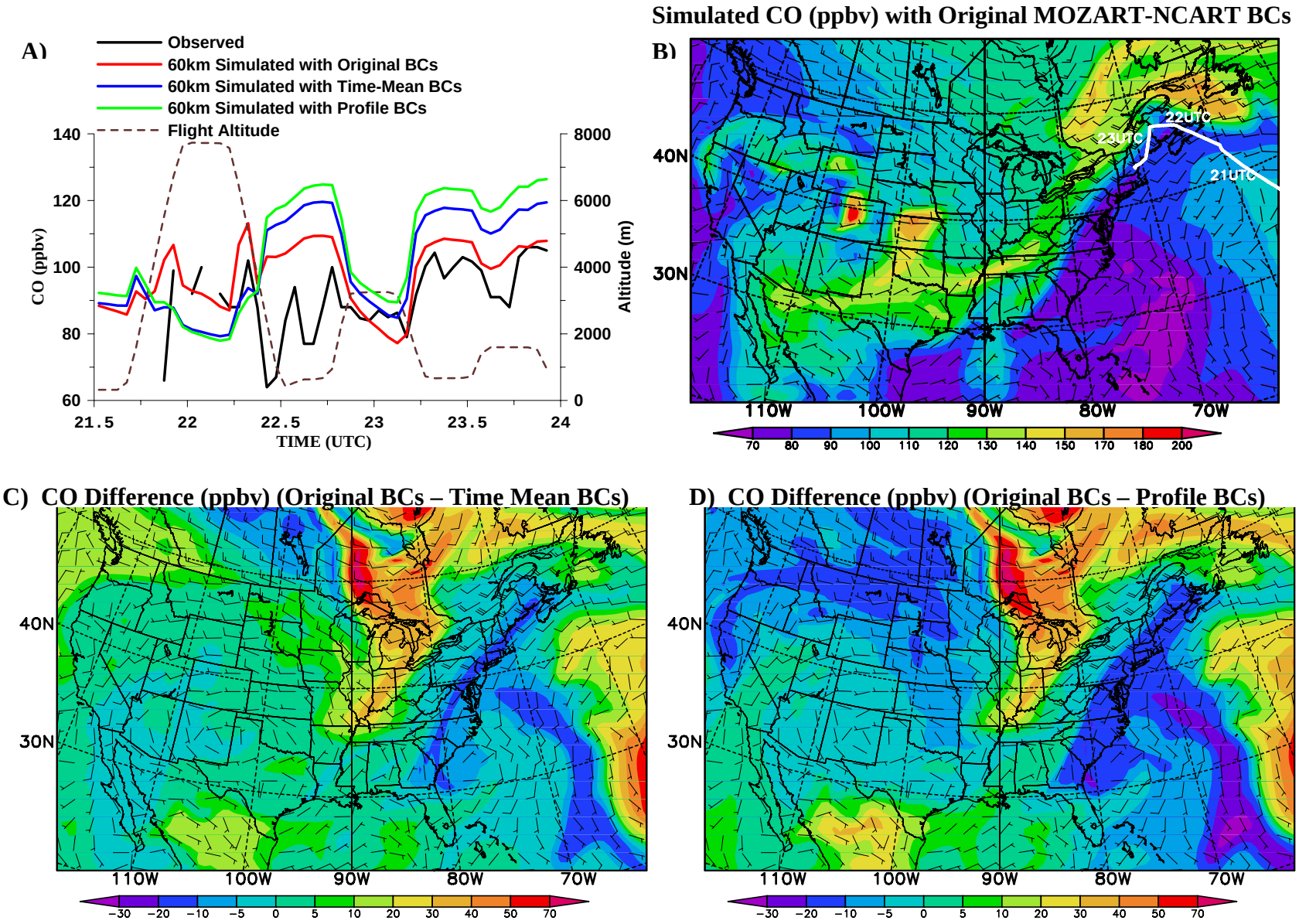

Figure 8. 60km simulated CO compared to the DC-8 flight observation on 07/31/2004. Plot B shows the simulated CO with original MOZART-NCAR BCs in the 3km layer, 0UTC, 08/01/2004. Plots C, D show the corresponding CO differences among the three simulations.

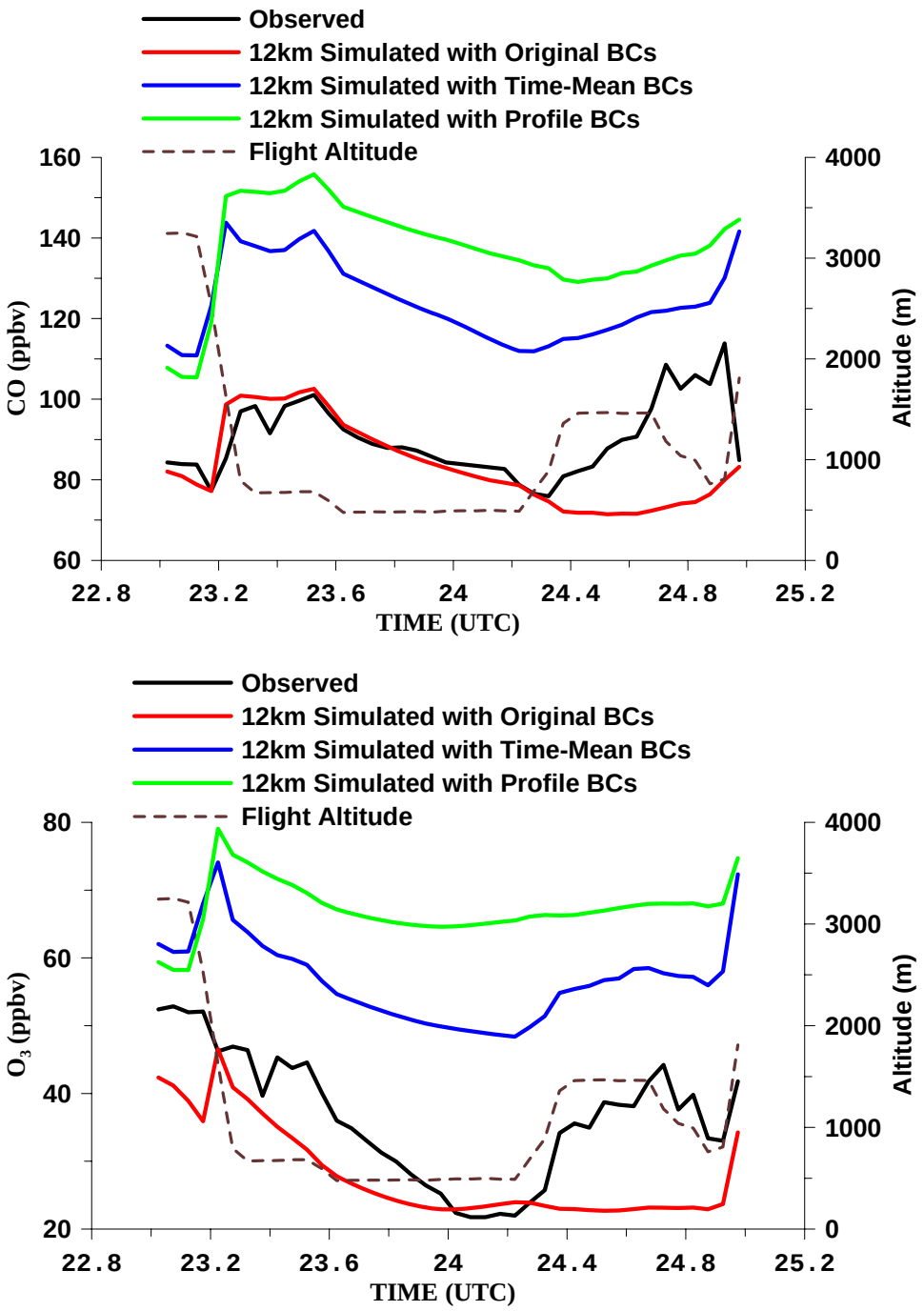

Figure 9. Observed and simulated CO and O_3 concentrations for the WP-3 flight 13 on 07/31- 08/01, 2004

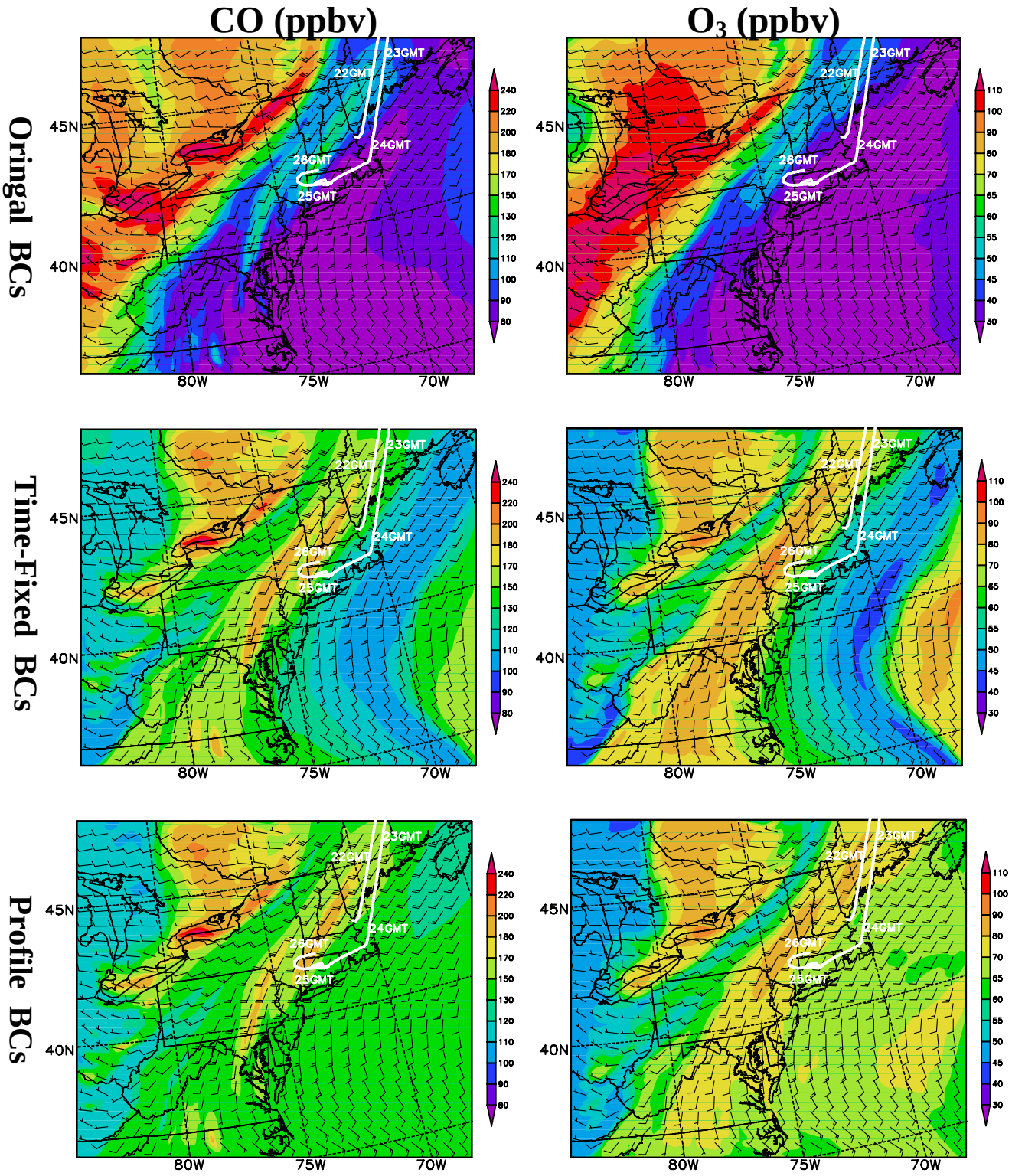

Figure 10. 12km simulated CO (left column) and O_3 (right column) concentrations in the 1km layer, at 0 UTC, 08/01/2004, driven by 3 different boundary conditions. The WP-3 flight path is shown in each plot.

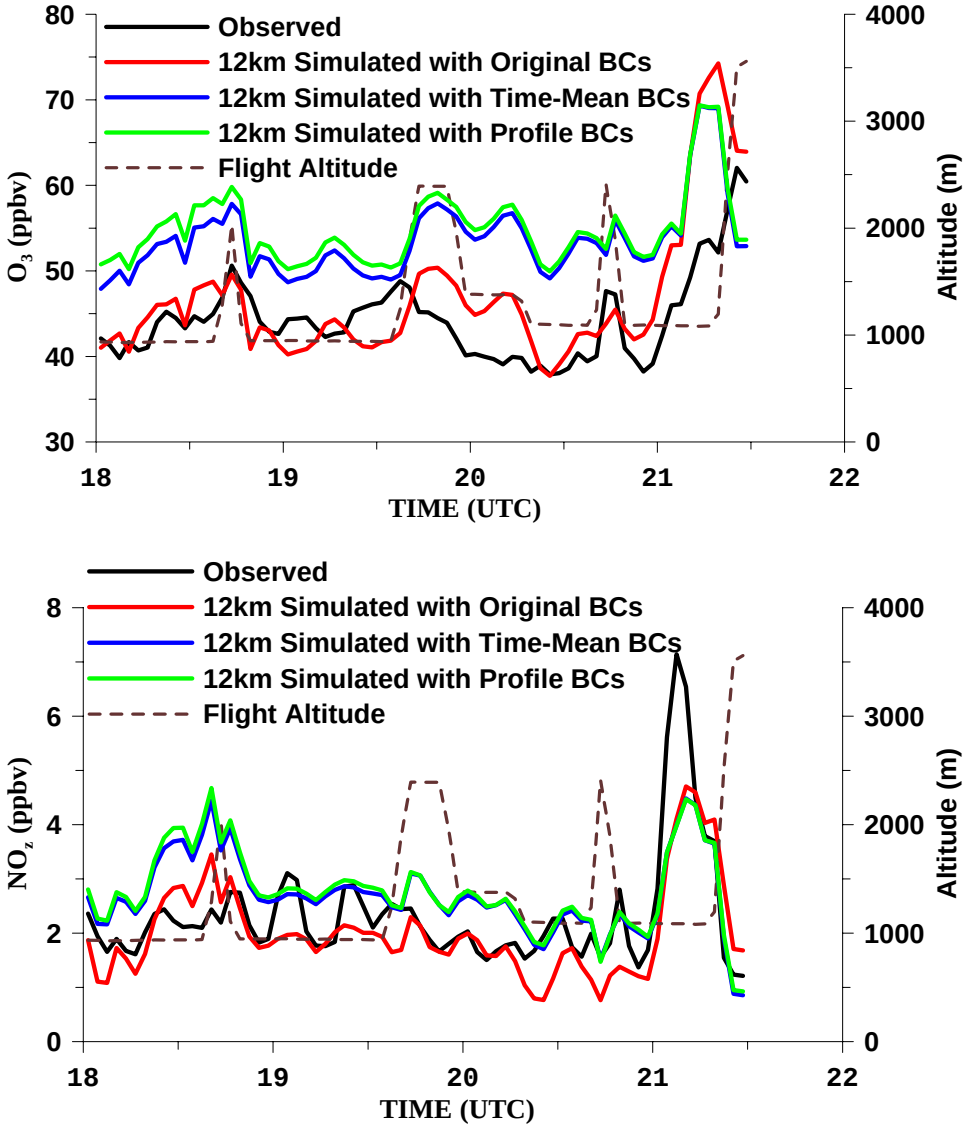

Figure 11. Observed and simulated O_3 and NO_z concentrations for the WP-3 flight 15 on 08/06/2004

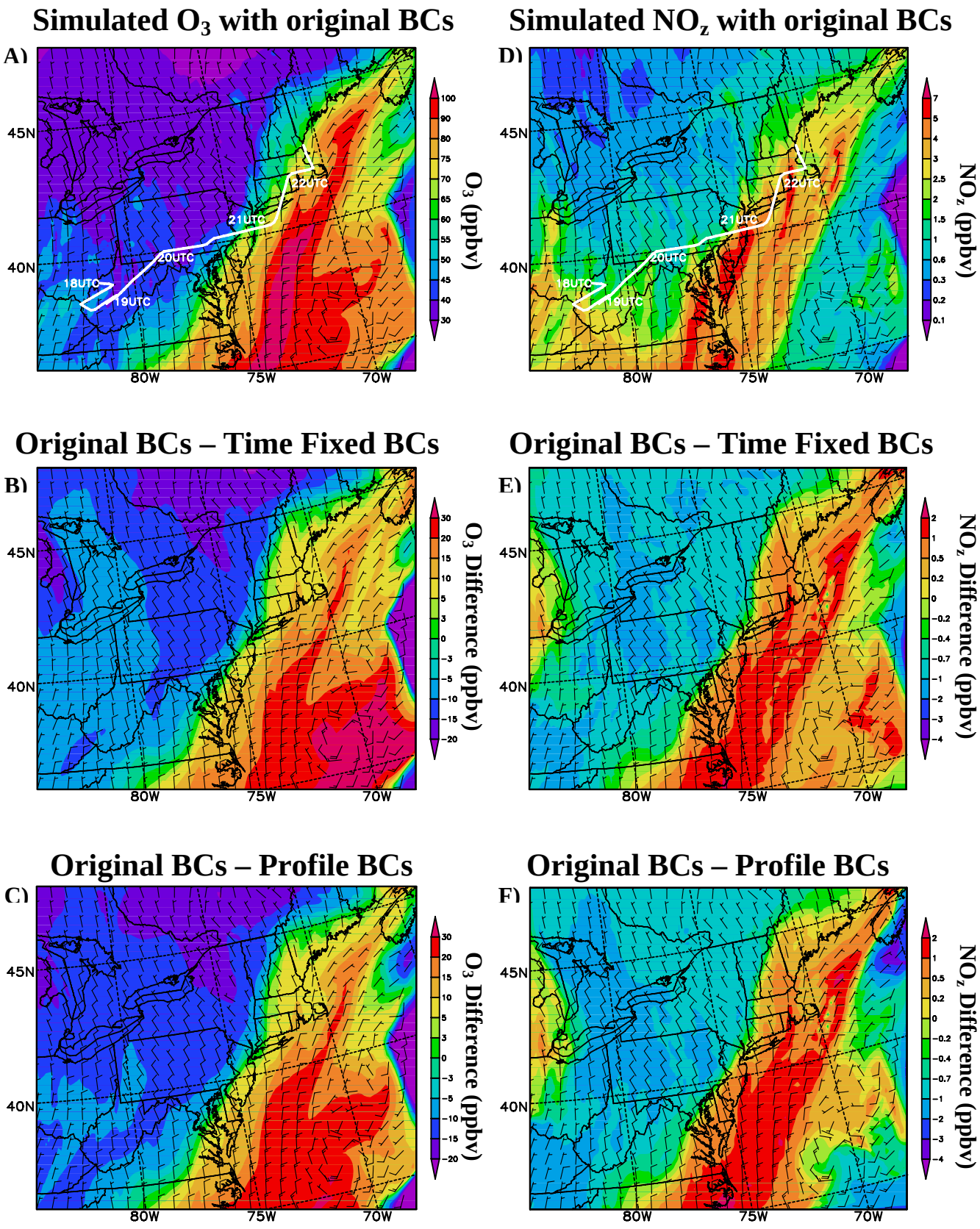

Figure 12. The 12km simulated O_3 and NO_z concentrations and their differences among the three simulations in the 1km layer, 18UTC, 08/06/2004.

NASA DC-8 Flight Paths during ICARTT Period

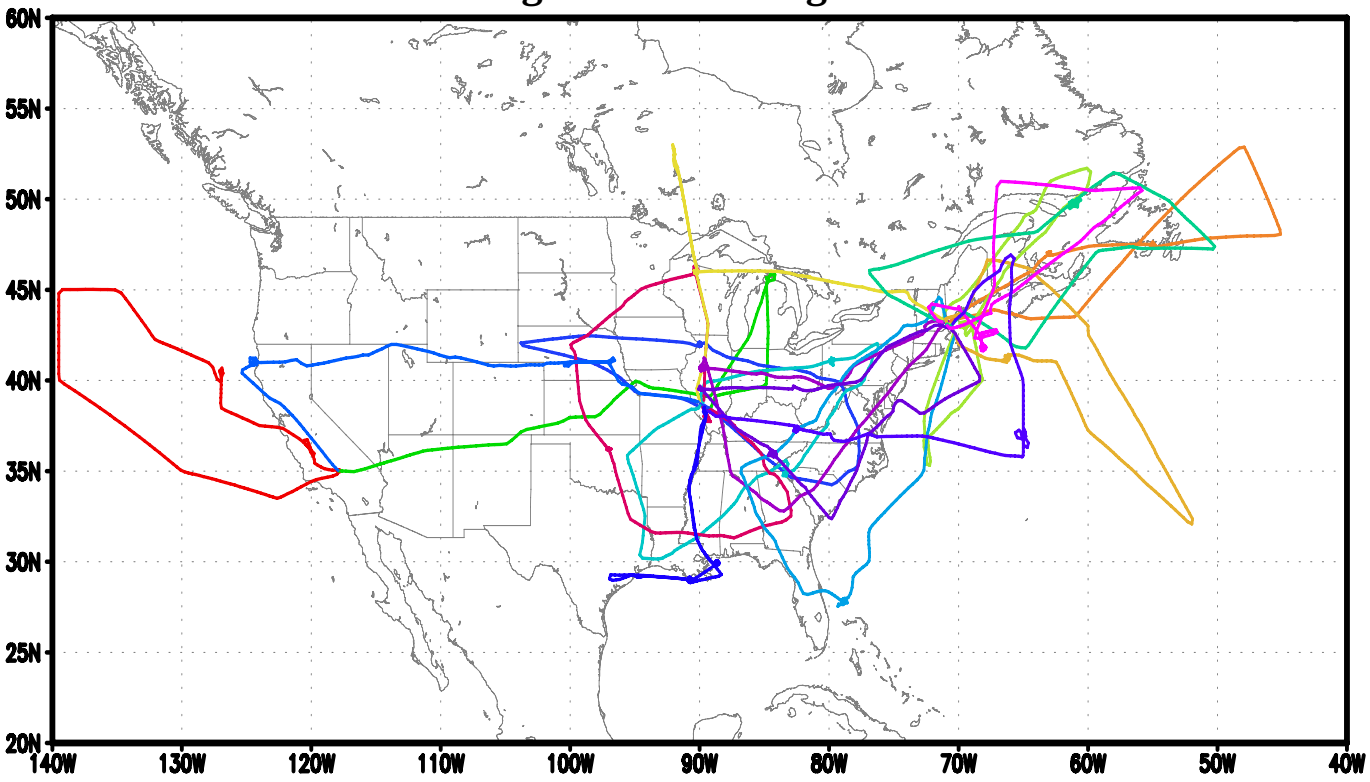

NOAA WP-3 Flight Paths during ICARTT Period

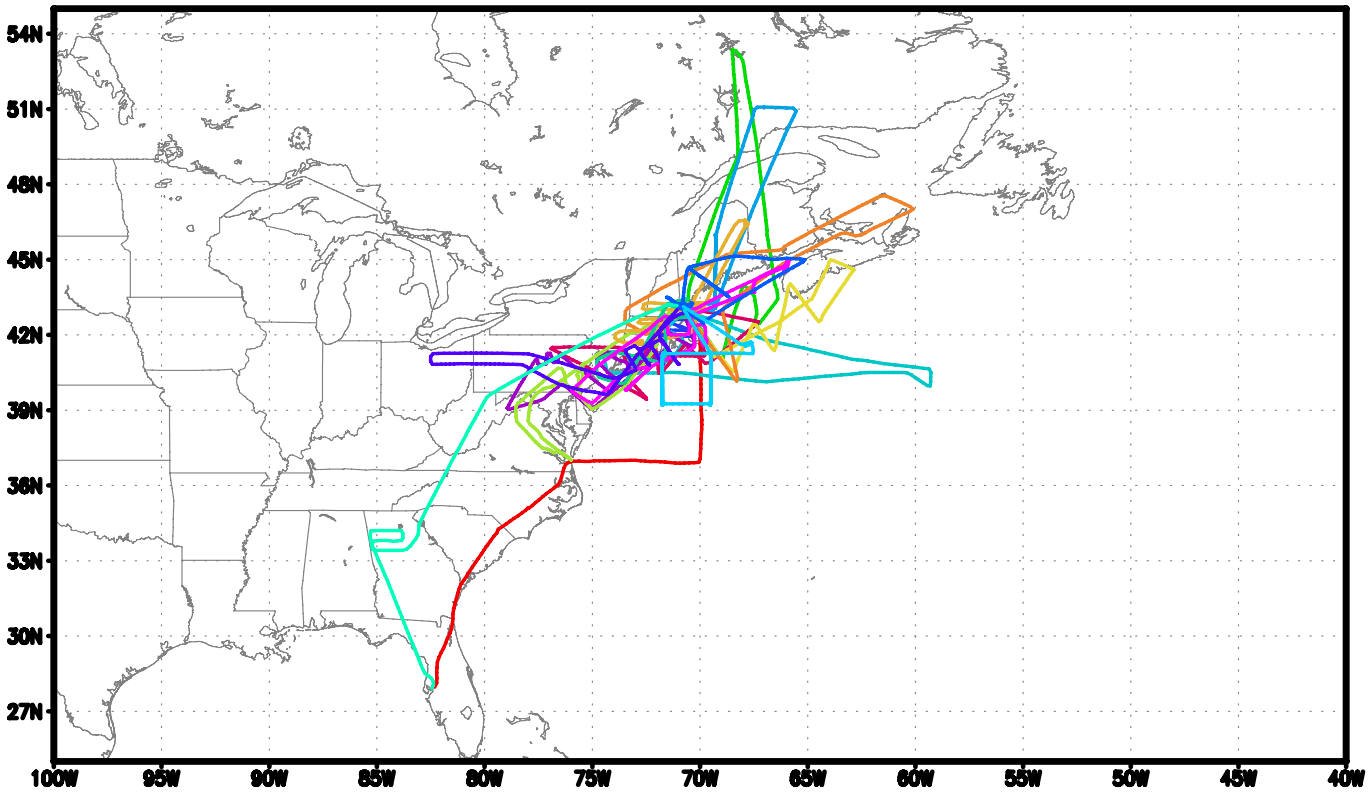

Figure 13. DC-8 and WP-3 flight paths during the ICARTT period

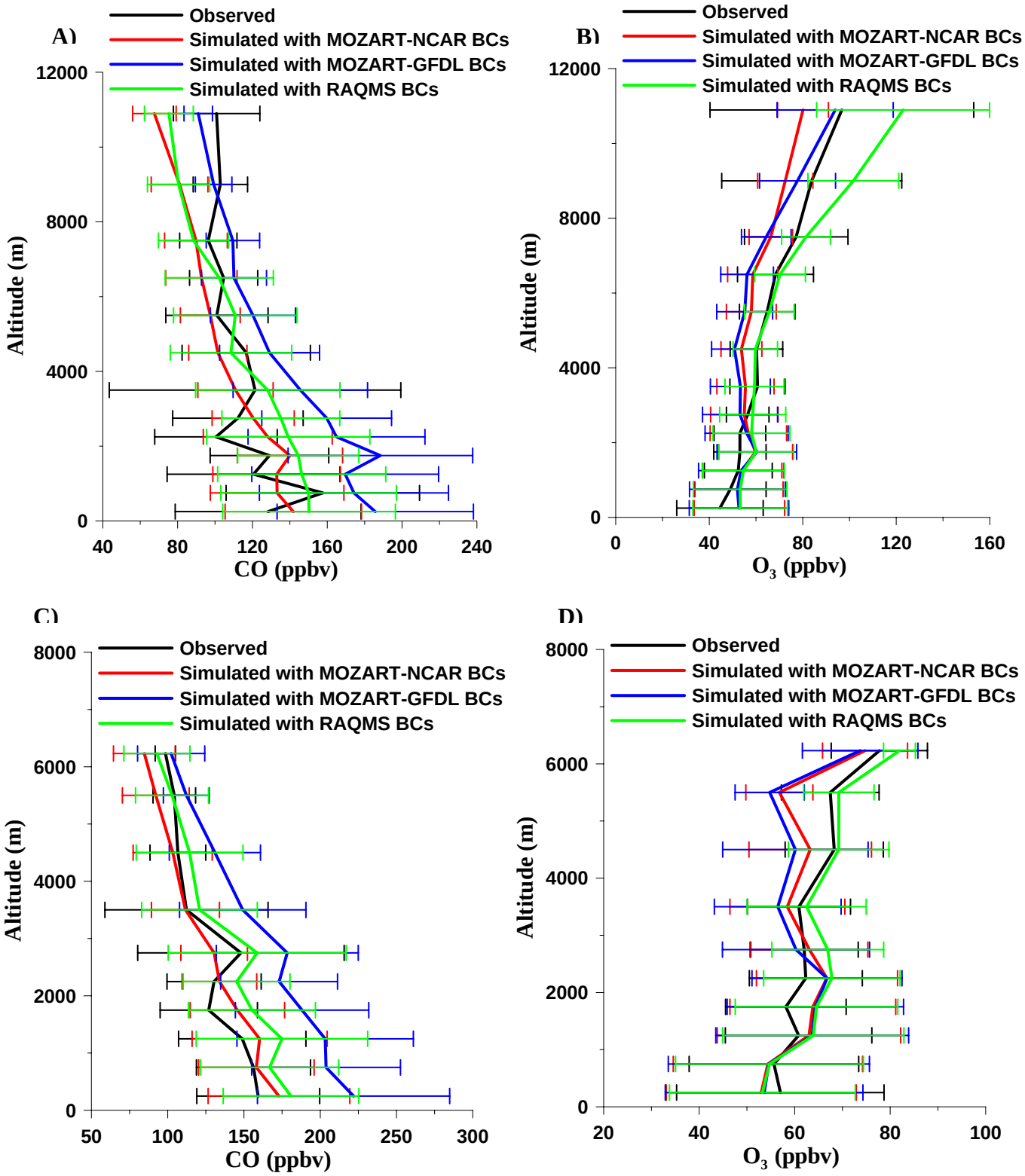

Figure 14. Observed and 60km-simulated CO and O_3 mean profiles and standard deviations for all DC-8 flights (A, B) and WP-3 flights (C, D)

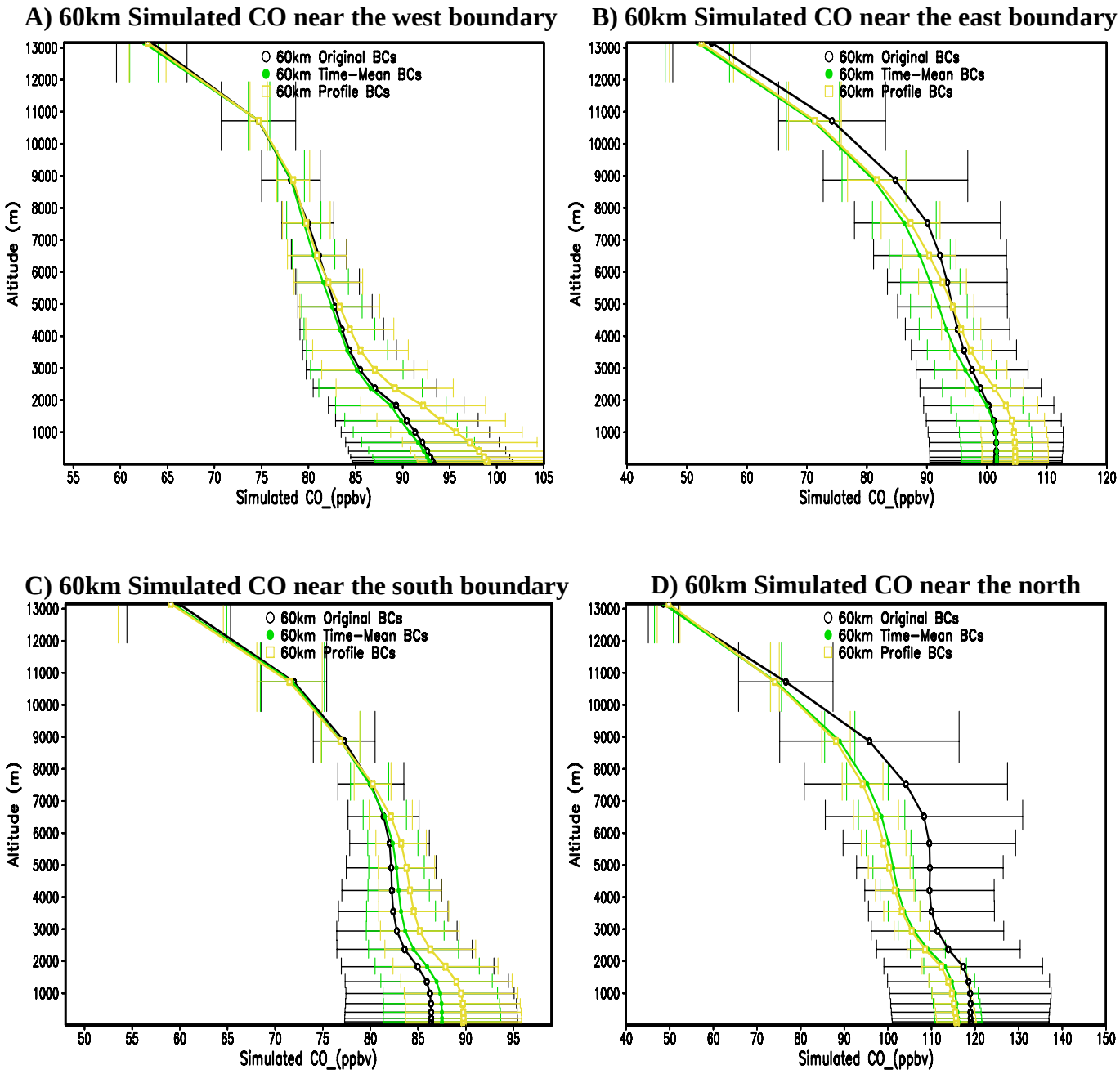

Figure 15. Simulated CO mean concentrations and standard deviation with original MOZART-NCAR, time-mean and profile boundary conditions over the grid lines that are 5 grid cells from west (A), east (B), south (C) and north (D) boundaries, respectively in the 60km domain.

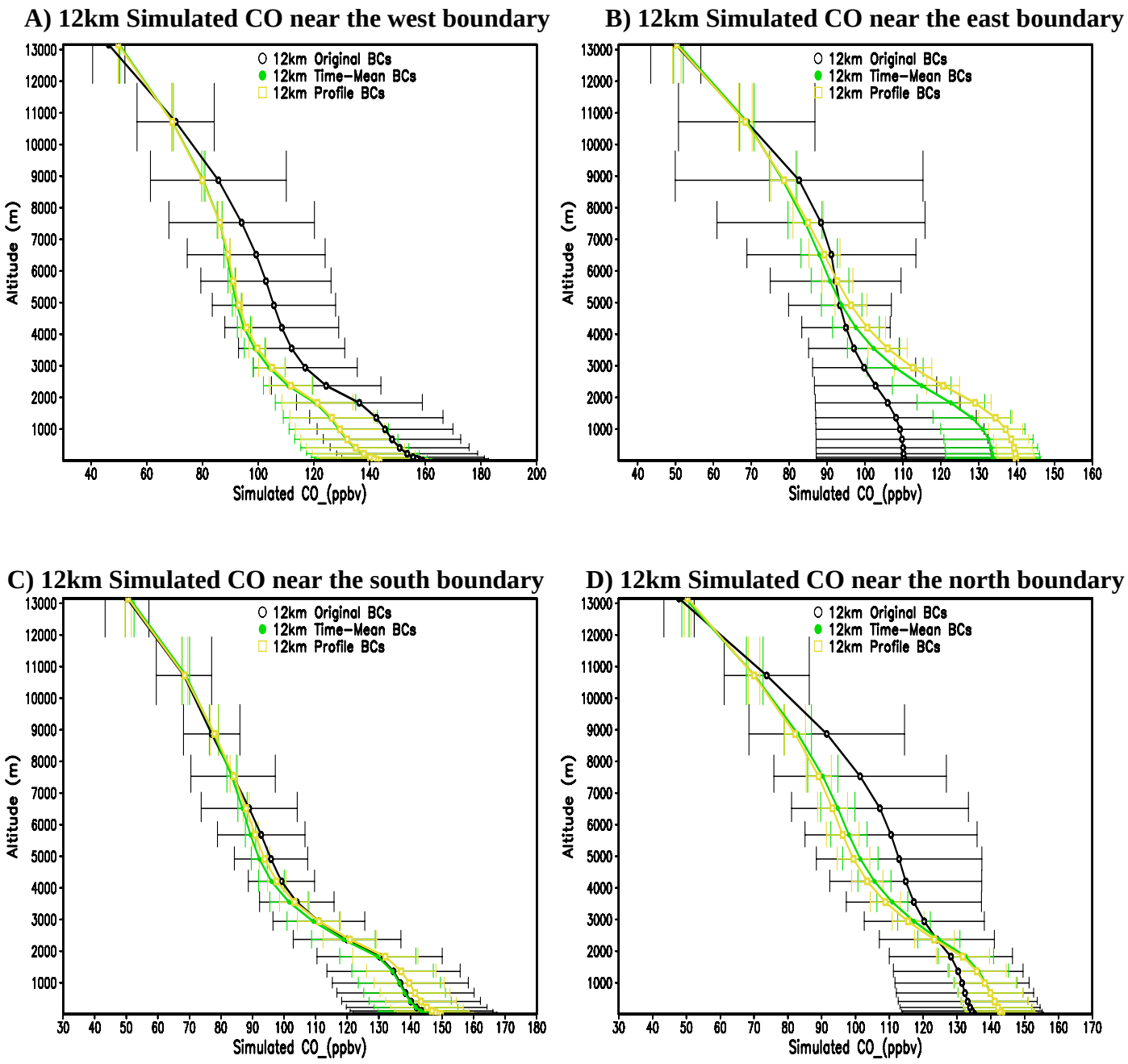

Figure 16. Simulated CO mean concentrations and standard deviation with original time-varied, time-mean and profile boundary conditions over the grid lines that are 5 grid cells from west (A), east (B), south (C) and north (D) boundaries, respectively in the 12km domain.

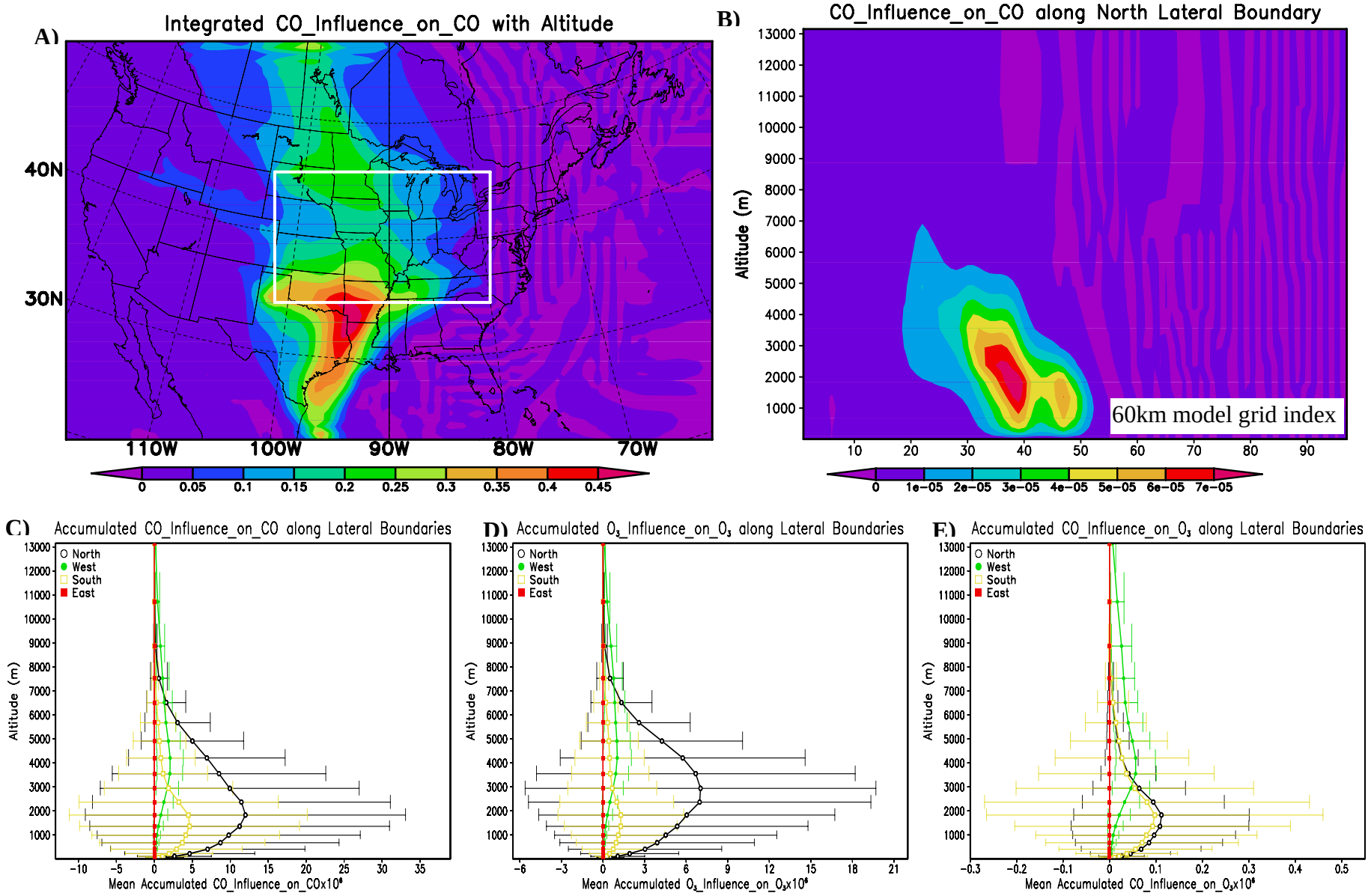

Figure 17. The influence function distributions: A) integrated with altitude B) north boundary and C), D), E) mean and standard deviations along the 4 lateral boundaries. The influence functions are integrated from July 19 to 24 for the target grid box with vertical elevation 1-4km shown in panel A.